Project work: Reservoir Engineering

Student Kristian Engen Eide

CO_2 induced calcite dissolution in Euville carbonate rock: Formation of wormholes

Rijswijk, The Netherlands, 30/11, 2011

NTNU
Norwegian University of Science and Technology
Faculty of Engineering Science and Technology
Department of Petroleum Engineering & Applied Geophysics

NTNU
Norwegian University of Science and Technology

Abstract

The present study is about a flooding experiment involving CO_2 saturated brine being injected into a calcite that was carried out prior to the study at the Shell Research Center in Rijswijk, Netherlands. Rock alterations induced by the interaction of acidic fluids are of particular interest for well stimulation, but are a major concern for CO_2 storage in aquifers or depleted reservoirs.

The main goal of this study was to thoroughly analyze the experimental data, carry out model calculations and get a better understanding of the reactive transport of CO_2 in carbonates and its affect on the rock properties. Of interest is the spatial distribution of calcite dissolution (dissolution pattern), in particular wormhole formation that was observed in the present experiment. A literature study on wormhole formation and the different dissolution regimes is included in the report to get an overview of important work done in previous studies and results that are relevant and might explain the results from the current experiment.

An Euville carbonate core sample from an outcrop in France was used in the experiment. The obtained results are consistent with what previous studies have shown. CT scans give evidence for the formation of a wormhole that penetrates the sample over the whole length. It is concluded that the reactive transport can be described as a reaction-controlled, convection predominant process.

A computer program has been developed to predict the solubility of calcite in CO_2-saturated brine at pressure and temperature conditions used in the experiment. The estimated solubility is by about a factor of 2 lower than the experimental results, suggesting a relatively high uncertainty on some of the input parameters such as dissociation constants or activity coefficients.

Analysis of CT images taken before and after CO_2 exposure of the rock allows for measuring the amount of dissolved calcite with a relatively high spatial resolution. The total amount of dissolved calcite as obtained from the CT images is consistent with the change in weight of the sample as well as estimates based on the calcium concentration in the effluent. Estimates of the wormhole dimensions can be obtained from the CT images as well.

The presence of localized features such as wormholes demonstrate that the reactive transport of CO_2 in carbonate rocks cannot be described by a 1D reactive flow equation; a more complex 3-dimensional approach that takes the microstructure of the rock into account is required.

Table of Contents

1 Introduction

The focus on reducing Green House Gas emission, in particular CO_2, has increased significantly over the last decades. One idea is to inject CO_2 into an aquifer or depleted reservoir. Acid treatments of wells or enhanced oil recovery (EOR) by gas injection have been done for several decades. Injection of CO_2 or other (aggressive) gases in the subsurface is not new to the industry. Acid treatments result in a reduction of the skin by exploiting the increase in solubility of rock mass when exposed to an acidic solution, creating a dissolution pattern, which increases permeability.

One special feature of CO_2 is that when dissolved in water, it reacts and forms carbonic acid. While CO_2 interaction might be beneficial for well stimulation, it might have adverse effects on reservoir and cap-rock integrity by causing, e.g., weakening of the rock.

A better understanding and the ability to predict that implications of CO_2 injection into the reservoir rocks is therefore of great interest. A vast number of studies have been conducted since the 1960s focusing on the development of models that describes the evolution of the pore structure and the matrix in general. Wormholes have been of particular interest because this turns out to be the optimum dissolution pattern for well stimulation. On a field scale, uniform dissolution is predicted for the far-field region, far away from the injection well.

The main goal and motivation behind the current study is to get a basic understanding of the interaction between CO_2-saturated brine and. The experiment discussed in this rock was the first in a series of experiments that will be carried out in the future. Simple models are used in an attempt of describing the experimental results. In the present work, we have (i) developed a simple program for predicting the solubility of calcite, (ii) modeled the concentration gradient within the core sample by a 1D reactive flow equation, and (iii) analyzed CT scans taken before and after CO_2 exposure of the rock.

In Chapter 2, the basic theory of CO_2 induced chemical reactions and reactive transport is presented, followed, in Chapter 3, by a literature review of important and relevant studies done in the past. The review is intended to help with the understanding and interpretation of the experimental results. The experimental setup and procedure are described in Chapter 4, and the results are presented in Chapter 5. In Chapter 6, the results are discussed and compared with results of model calculation. Finally, conclusion and an outlook are presented in Chapter 7.

The experimental work, measurements and CT-scans are done by researchers at the Shell Research Center in Rijswijk, Netherlands. The analytical work has been performed by the author.

2 Theory

2.1 Chemical reactions

When introducing CO_2 and water, dissolution occurs, which can be describes by [1]

$$CO_{2(g)} \rightarrow CO_{2(aq)} \tag{1}$$

Further on, CO_2 reacts with the water and forms carbonic acid, which is a weak diprotic acid. The following equations describe the reaction as well as the dissociation of the acid.

$$H_2O + CO_{2(aq)} \rightarrow H^+ + HCO_3^- \tag{2}$$

$$HCO_3^- \rightarrow H^+ + CO_3^{2-} \tag{3}$$

Dissolution of gas and the associated acid dissociations in aqueous solutions is assumed to be at equilibrium thus the equilibrium and dissociation constants for the above equations can be defined as

$$K_H = \frac{m_{CO_{2(aq)}}\gamma_{CO_{2(aq)}}}{P_{CO_2}\gamma_{CO_{2(g)}}} = \frac{a_{CO_{2(aq)}}}{f_{CO_{2(g)}}} \tag{4}$$

$$K_1 = \frac{a_{H^+}a_{HCO_3^-}}{a_{CO_{2(aq)}}a_{H_2O}} \tag{5}$$

$$K_2 = \frac{a_{H^+}a_{CO_3^{2-}}}{a_{HCO_3^-}} \tag{6}$$

where K_H is Henry's constant, K_1 and K_2 are the dissociation constants, a_i is the activity of species i, and m, γ and f denote molality, activity coefficient and fugacity, respectively. The reaction described in equation (2) is a combination of the reaction between CO_2 and water forming carbonic acid, H_2CO_3, and the first dissociation of this. The reason for this is that at equilibrium, CO_2 is the preferred state thus the concentration of H_2CO_3 can be neglected in the mass balance.

The conversion into an acid in water is an important feature of CO_2. Acidic solutions are known to enhance dissolution of certain minerals. This applies particularly to carbonates such as $CaCO_3$. In pure water $CaCO_3$ is more or less insoluble. The dissolution can be described by equation (7) with the corresponding equilibrium equation (8).

$$CaCO_3 \leftrightharpoons Ca^{2+} + CO_3^{2-} \tag{7}$$

$$K_{sp} = \frac{a_{Ca^{2+}} a_{CO_3^{2-}}}{a_{CaCO_3}} \quad (8)$$

Again, a denotes the activity, which for solids are defined as 1. K_{sp} is the dissociation constant, or more commonly referred to as the solubility constant, which is dependent of both temperature and pressure, the latter being of less importance. Having that CO_3^{2-} is the conjugate base to a weak acid CO_3^{2-} prefers to associate with H^+. The association can be described as the reverse of equation (7). According to Le Chatelier's principle [2], a system that experiences disturbance in the equilibrium shifts in order to counteract the changes. Therefore, as H^+ is spent and CO_3^{2-} consumed, more $CaCO_3$ is dissolved to counteract, hence an increase in the solubility.

There is also dissociation of water that has to be taken into account:

$$H_2O \rightleftharpoons H^+ + OH^- \quad (9)$$

$$K_w = \frac{a_{H^+} a_{OH^-}}{a_{H_2O}} \quad (10)$$

Here, K_w is therefore defined as the dissociation constant of water, which is quite important when acid reaction in water is studied. The activity of pure water is 1, leaving the K_w to be the product of the activity of H^+ and OH^-. The K_w is especially important during measurements of pH. At standard conditions $K_w=10^{-14}$.
The activity is defined as the effective concentration of a solute and is related to the absolute concentration by the activity coefficient, γ. Ideally, activity coefficients are assumed equal to 1. However, it is the chemical potential that determines the activity. Chemical potential is the potential that a substance has to result in a change in a system. The chemical potential is dependent of pressure and temperature, thus the activity coefficient can vary significantly from unity. Activity is dependent of temperature, pressure and composition of the mixture among other things through the chemical potential. Fugacity, introduced earlier, is referred to as the activity for gases. It is therefore evident that the activity coefficient must be included to achieve accuracy in equilibrium calculations. The sensitivity to activity change is illustrated and addressed in the discussion section.

Predicting the amount of dissolved calcite is of great interest. The equilibrium equations alone are not enough in order to make estimations. Electric neutrality for the solution applies, and can be described by

$$2Ca^{2+} + H^+ = HCO_3^- + 2CO_3^{2-} + OH^- \quad (11)$$

One more equation is needed, which is dependent on whether it is an “open” or “closed” system. Here, the term “open” indicates that the reaction is exposed to an unlimited source of CO_2, while a “closed” system has only the initial amount of CO_2.

A closed system is used in the current experiment. Mixing of CO_2 and brine is done in an autoclave, determining the initial concentration of CO_2 in the system. The saturated brine is then injected into the rock without being exposed to a source of CO_2 after mixing. We refer to the experiment chapter for further description. The final equation needed in order to estimate the dissolution is based on the atomic carbon balance. Each molecule of dissolved calcite adds one carbon atom to the solution, thus

the final number of carbon atoms in the solution is equal to initial number added by the initial CO_2 plus the dissolved calcite.

$$Ca^{2+} + CO_{2,i} = CO_{2,aq} + H_2CO_3 + HCO_3^- + CO_3^{2-} \quad (12)$$

Although Henry's constant is not required in the actual dissolution process it may be used in the mixing process in order to determine the initial saturation concentration.

2.2 Reactive transport

Reactive transport is the transport of mass in a reactive system. The kinetics of reactive transport in a porous rock is influenced by three different mechanisms [3]: advection, diffusion (molecular diffusion and mechanical dispersion) and reaction. Advection is the transport of molecule caused by the motion of fluid, in which a pressure gradient often may be a drive mechanism. Similar to heat, which is controlled by a heat gradient, concentration gradient is the driving force in molecular diffusion. A system without any external acting forces will eventually result in complete mixing. The reaction part of the kinetics does not induce any physical transportation. However, reactions do have a significant indirect effect on the transportation. Intuitively, a reaction causes changes in concentration and therefore gives rise to concentration gradients and diffusion.

Transportation of reactants is essential in order for the reactions above to occur. The fundamental description of the change in time can be made by the following equation. In general, this is the mass balance or continuity equation:

$$\frac{df}{dt} = \frac{\partial f}{\partial x}\frac{dx}{dt} + \frac{\partial f}{\partial t} \quad (13)$$

Here, f represents e.g. the concentration. The first term on the right side describes the change of f in time caused by a gradient along the x direction ($\frac{\partial f}{\partial x}$) and flow velocity ($\frac{dx}{dt}$). The second term is the change in time at a certain point caused by e.g. reaction.

This equation is applicable for the description of reactive transport. A simplified, though illustrative example in 1D can be made by [3]:

$$\frac{\partial C}{\partial t} = -\phi v\frac{\partial C}{\partial x} + \phi D\frac{\partial^2 C}{\partial x^2} + Ak(1 - \frac{C}{C_{eq}}) \quad (14)$$

where ϕ is the rock porosity, C is the concentration of the respective solute, v is the Darcy velocity, D the diffusion constant, A the surface area of the grains per unit of volume, k the reaction rate coefficient and C_{eq} the solubility limit. The k value for the reaction, which is of particular interest in the current report, is in the range of ~10^{-8} mol/cm^{2}s [4], [5], [6]. Basically, the equation can be directly related to the continuity equation, and is constituted by the three mechanisms mentioned above. The first and second term are describing the advection and diffusion of the molecules in the x direction, respectively. These two terms are responsible for the change in concentration, flow and concentration gradients along the x direction, while the latter term of the equation describes the reaction rate, which is the change in time at a given position. The equation is often referred to as an advection-diffusion-reaction (ADR) equation. Note that the reaction rate term is significantly simplified by assuming a

first order reaction. In reality, the reaction might be of higher order as seen by the definition further down.

There are two different controlling regimes governing the reaction and the system in general, named transport-controlled (reaction-limited) and reaction-controlled (transport-limited). These regimes correspond to whether it is the transport of the reactants or the reaction rate that is the controlling factor. "Transport-controlled" implies that the transportation in the axial direction is too fast for the chemical reaction to reach equilibrium, resulting in an undersaturated effluent. On the contrary, "reaction-controlled" implies that the reaction rate is fast enough to ensure fully buffered solution, hence the transportation rate has no impact on the saturation state of the effluent. If the system is transport-controlled, it might be either convection predominance or diffusion dominated. As will be discussed later, an understanding of the reactive flow regime is of great importance for a more detailed description and understanding of the dominant dissolution regime.

Equation (14) is applicable to investigate whether the system is transport controlled or reaction controlled on a macroscopic scale, neglecting processes on a microscopic scale such as diffusion within a pore. The macroscopic approach might be sufficient in most cases. Diffusion at a pore scale, which described the transportation mechanism from the center of a pore to the pore wall, becomes more important for large diameter pores and high flow rates (e.g. close to an injector well). As will be presented in the literature study chapter, Schechter and Gidley[7] described the change in pore size due to leaching by a capillary tube approach. This approach implies a micro scale study where the radial diffusion is introduced to the mass balance equation.

It should also be noted that time dependent changes of the porosity, permeability and specific surface area (smoothening effects) have to be taken into account in a proper evaluation of the reactive transport. The reaction rate describes how fast a reaction or conversion occurs. The general definition of the rate for the following reaction

$$aA + bB \rightleftharpoons pP + qQ \tag{15}$$

is

$$r = -\frac{1}{a}\frac{d[A]}{dt} = -\frac{1}{b}\frac{d[B]}{dt} = \frac{1}{p}\frac{d[P]}{dt} = \frac{1}{q}\frac{d[Q]}{dt} \tag{16}$$

In our case, for surface reaction, the unit of the reaction rate is [mol m^{-2} s^{-1}]. The reaction rate is dependent of several factors. Intuitively, factors such as the number of the species and their physical state are some of the most important ones. The physical state dependence implies a dependency to the parameters that affects how frequent the components interact. Temperature, concentration, pressure and order are some significant parameters.

To relate the last term in the continuity equation to the reactive flow equation, which is as mentioned the reaction rate, the following definition may be used.

$$\frac{\partial f}{\partial t} = Ar = Ak[A]^x[B]^y \tag{17}$$

This equation involves the reaction orders, x and y, which must be determined experimentally. k is the rate coefficient in which all dependencies are included, whereas [A] and [B] represents the concentration of component A and B. From the definition, we see that the rate term in equation (14) is a special case, and indeed quite simplified in the reactive transport equation.

There are in particular two dimensionless numbers that are frequently referred to during the study of reactive transport. These are the Péclet number (Pe) and the Damköhler numbers (Da). The Péclet number relates advective and diffusive transport rates, whereas the Damköhler numbers relates the chemical reaction rate and the advective rate. Since convective transport involves both advection and dispersion, two different Damköhler numbers are used depending on the dominant mechanism. The numbers are defined as follows:

$$Pe = \frac{vL}{D} \tag{18}$$

$$Da_I = \frac{AkL}{\emptyset v C_{eq}} \tag{19}$$

$$Da_{II} = PeDa_I = \frac{AkL^2}{\emptyset D C_{eq}} \tag{20}$$

where Da_I and Da_{II} are respectively the advection and diffusion Damköhler numbers. Furthermore, L is the characteristic length, v the velocity, D the mass diffusion coefficient, k the chemical reaction rate constant and C_{eq} the concentration at equilibrium. As will be discussed later, these numbers are quite important in the quantification of the dominant dissolution regime.

2.3 Dependencies for the equilibrium-constants.

As mentioned earlier, the chemical potential determines the activity of the components, and that the potential are dependent on parameter such as temperature and pressure. Temperature has the biggest effect on the chemical potential for components in a solution. By the definitions presented earlier, the equilibrium constants are therefore temperature dependent. On the contrary, pressure dependence is often neglected due to the weak effect that changes in pressure on a relatively small scale has for liquid-phase reactions. This assumption is also applied in our case except for Henry's law that describes the solubility of CO_2 gas in water. The solubility of CO_2 in water is addressed further down.

There have been many experiments and studies on the temperature dependence of chemical reactions, mostly for temperatures ranging from 15 to 50 ^{0}C, while less is published for higher temperatures. Extensive work has been done by Plummer and Busenberg [8] in critically evaluating and comparing previous work, and they find the following temperature dependencies:

$$Log(K_C) = -171.9065 - 0.077993\,T + \frac{2839.319}{T} + 71.595 \log_{10}(T) \quad \text{for} \quad 273\ \text{K} < T < 363\ \text{K} \tag{21}$$

$$Log(K_A) = -171.9773 - 0.077993\,T + \frac{2903.293}{T} + 71.595\log_{10}(T) \quad \text{for} \quad 273\ \text{K} < T < 363\ \text{K} \qquad (22)$$

$$Log(K) = a + bT + \frac{c}{T} + d * \log_{10}(T) + e/T^2 \quad \text{for} \quad 273\ \text{K} < T < 523\ \text{K} \qquad (23)$$

where T is in Kelvin, and a, b, c, d and e are coefficients given in Table 1for the respective reactions. The latter equation applies for Henry's constant (K_H) and the dissociation constants (K_1 and K_2). Equation (23) is also used by the numerical simulator *ToughReact,* a simulator based on *Tough2* coupled with a geochemical module [9], to regress input equilibrium constants as a function of temperature.

Calcium carbonate exists in different forms in nature depending on the geological time and conditions the carbonate was formed in. The three forms are calcite, being the most dominant one, aragonite and vaterite. The latter form is the least stable and converts to the other forms in contact with water. We know that Euville mainly contains calcite, however a comparison of calcite and aragonite is done and can be seen in Figure 1 together with the plots of the equilibrium and temperature dependencies of the dissociation constants.

Table 1: The different coefficients for the temperature dependency equations for the dissociation constants.

Constant	a	b	c	d	e
K_H	108.3860	0.01985076	-6919.530	-40.45154	669365.0
K_1	-356.3094	-0.06091964	21834.370	126.83390	-1684915.0
K_2	-107.8871	-0.03252849	5151.790	38.92561	-563713.9

As can be seen from the comparison of the solubility constants for calcite and aragonite, the difference is quite small and the temperature dependence is similar, thus the uncertainty on which mineral is present will not affect the results in a significant way. For the present study, we assume that the rock is composed of calcite.

From the definitions of the solubility constant and the dissociation constants, we can expect that the solubility of $CaCO_3$ increase with an increase in K_{sp} and K_1, respectively, whereas an increase in K_2 will result in a decrease in solubility. This understanding correspond to the observations and measurements presented by Plummer and Busenberg [8]

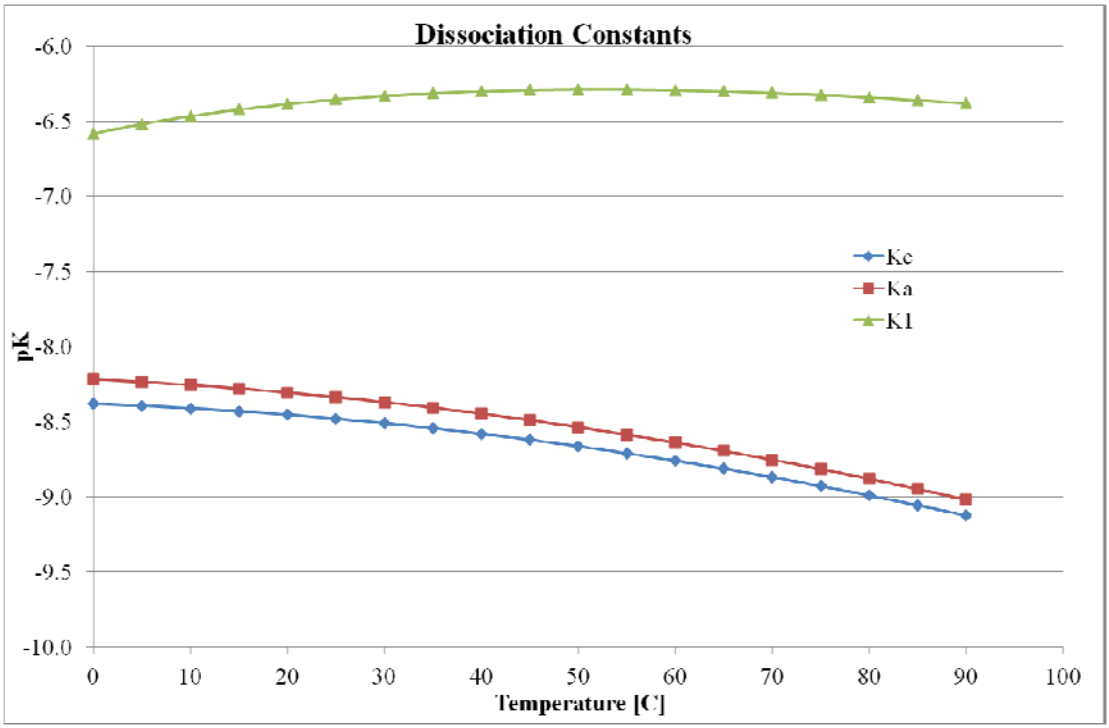

Figure 1: Dependence of the dissociation constant with respect to temperature.

It should also be noted that the dependence of the water dissociation constant on temperature is quite significant and must be taken into account when making accurate measurements of acid reactions in water. The plot below (Figure 2) shows the temperature dependency of K_w.

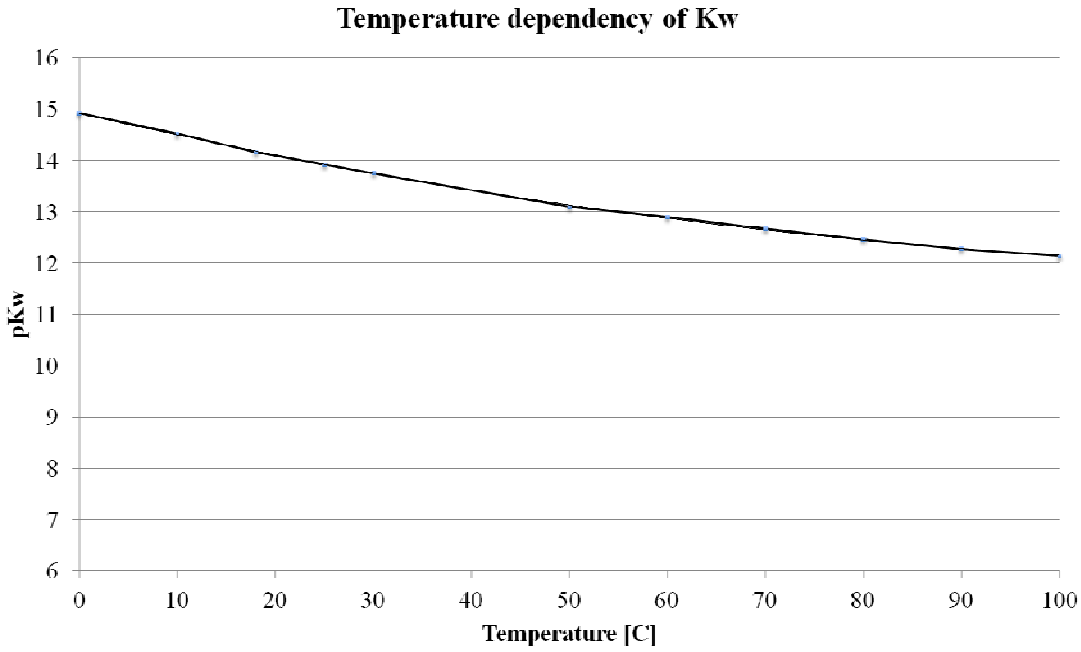

Figure 2: Dependence of Kw with respect to temperature.

2.4 CO2 solubility in water

As mentioned above, Henry's constant shows significant dependence on both temperature and pressure, making the estimations of the solubility of CO_2 in water at different conditions significantly more complex. According to the definition of Henry's constant, keeping the temperature constant and varying the pressure should result in a linear relation of the solubility. However, it is evident from the solubility curves of CO_2 in water presented in Figure 3 that a linear relation between the different pressure curves does not apply. This indicates that the constant also depends on pressure. Plummer and Busenberg's [8] studies on the temperature dependence of the different dissociation constants included Henry's constant. The pressure was however always kept constant thus the derived relation only applies to one atmosphere.

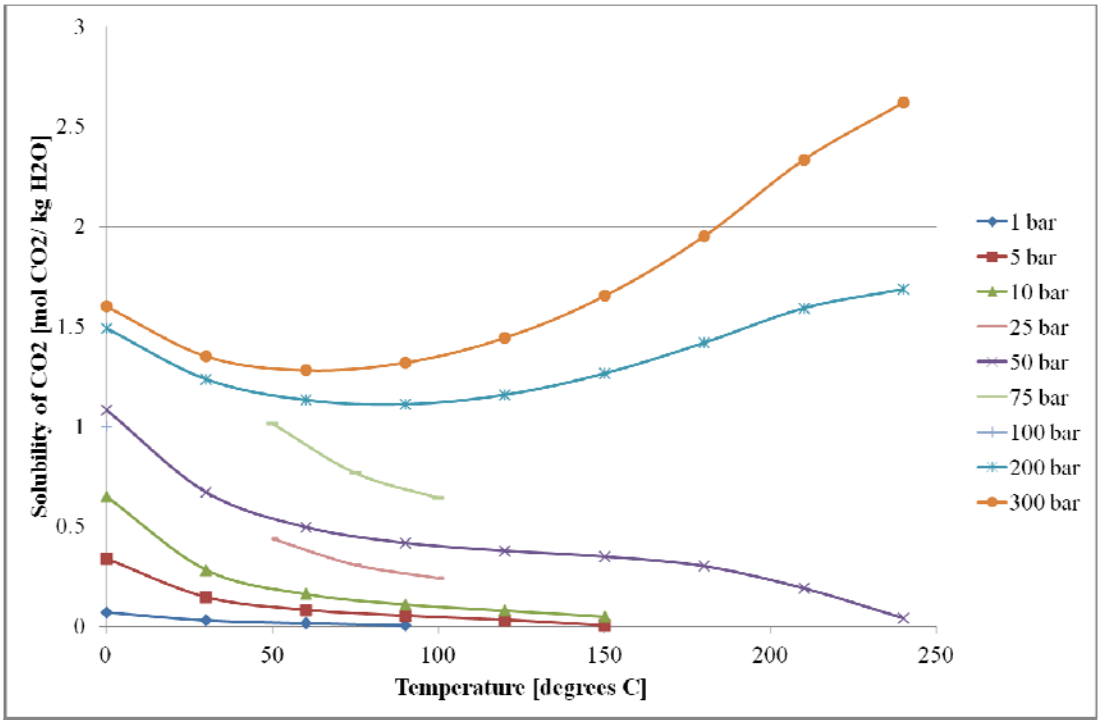

Figure 3: Solubility of CO_2 in water at different temperatures and pressures. [10], [11]

3 Literature Study

Chemical interaction between rock and fluid has long been of great interest, not only for petroleum engineering. The reaction between carbonates and CO_2 as both (supercritical) gas and dissolved in brine has been of particular interest. The increased focus on reducing CO_2 emissions has enhanced the idea of injecting CO_2 in saline aquifers or depleted reservoirs. Better knowledge and understanding of the interaction between rock and fluid is therefore becoming more and more important. Previous studies hold information on possible sources of error and weaknesses, but also recommendations on adjustments, which might improve accuracy and the reliability of the results. The experiment described in this project is dealing with CO_2-saturated brine and its interaction with calcite, thus the main focus in this review of previous studies will be on topics relevant for this case.

What makes CO_2 so special is the feature of forming an acid on water as brine, which enhances the solubility of carbonates significantly. Already in the 1960s, the fundamental understanding of the interaction between CO_2 saturated brine and carbonates were well established and the interest on the topic increased rapidly. Pioneering work was done by Schechter and Gidley [7] at this time. They were one of the first groups who tried to explain the evolution of the pore-size distribution in a carbonate matrix during exposure to acidic brine. The possible pore structure modification is of great significance regarding hydraulic properties (permeability) but also geomechanical properties and the integrity of the formation. Altering these properties might result in severe issues. The results from their publication "The change in pore size distribution from surface reaction in porous media" was important for later studies and is also relevant for the experiment addressed in this report. A review of this paper is therefore appropriate. The overall motivation behind this work was the widespread and increasing use of acid for well stimulation. The intention of the study was to give a fundamental understanding of the acid-rock interaction and a basis for estimations of changes the pores are subjected to. This is required for proper design of acidizing. Their work focuses on the questions: To what extent will this dissolution of solid enhance the permeability of the reservoir? How far will the acid penetrate? What is the effect of flow rate? Does the reaction rate influence the results?

In their publication, a rather extensive derivation is presented, in which the description of the pore evolution during acid exposure is one of the final results. The model, which they base their derivation on, is basically a capillary model in which a solid containing a matrix of randomly distributed and interconnected holes makes up the porous medium. The pores are represented by a large number of short cylinders assumed to be geometrically similar. Important parameters are all interpreted using the capillary model. Figure 4 shows the idealized model. However, in a subsequent study, Christman and Edgar [12] applied the same model, which led to the recognition of some limitations of the model with respect lack of pore interactions.

Schechter and Gidley start off by defining a pore-size density function, $W(A,x,L,t)$, so that $W(A,x,L,t)\times dA\times dL\times w^2\times dx$ is the number of pores having an area and length between A and A + dA and L and L + dL, respectively, in the volume w^2dx. Knowing W makes the calculation of different parameters possible, porosity being one of them:

$$\phi(x) = \iint_0^\infty A \cdot L \cdot W(A, L, x, t) \cdot dA \cdot dL \tag{24}$$

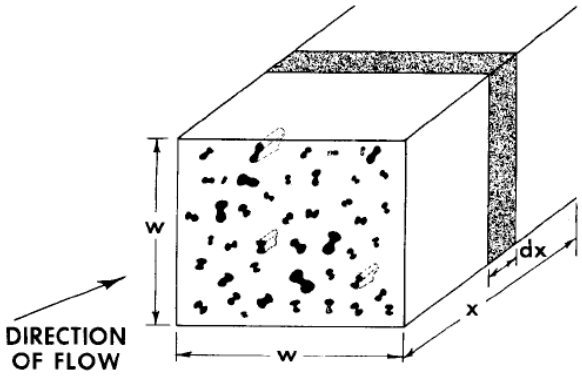

Figure 4: Idealized model of a porous media.[7]

Considering a plane perpendicular to the x-axis, permeability could be estimated by determining the total volume of fluid passing through it. They assumed laminar flow, which yields:

$$\bar{v} = \epsilon A \tag{25}$$

where ϵ is a factor that depends on the pressure gradient $\frac{\partial P}{\partial x}$, viscosity ($\mu$), and pore geometry:

$$\epsilon = -(geometric\ factor)\frac{1}{\mu}\frac{\partial P}{\partial x} \tag{26}$$

Each pore is geometrically equal, thus ϵ is equal implying that the volumetric flow is given by:

$$q = \epsilon w^2 \iint_0^\infty A^2 \cdot L \cdot W(A, L, x, t) \cdot dA \cdot dL \tag{27}$$

Combining the equation above with Darcy's Law, the permeability evolution can be found by:

$$\frac{K(x,t)}{K(x,o)} = \frac{\mathrm{q(t)}}{\mathrm{q(t=0)}} = \frac{\iint_0^\infty A^2 \cdot L \cdot W(A, L, x, t) \cdot dA \cdot dL}{\iint_0^\infty A^2 \cdot L \cdot W(A, L, x, 0) \cdot dA \cdot dL} \tag{28}$$

Further simplifications were needed in order to develop a mathematical expression for the pore density evolution. What Schechter and Gidley did was to extract the function, P(L), which describes the fraction of pores having a length between L and L + dL, from the density function.

$$W(A, L, x, t)w^2 dA dL dx = \eta(A, x, t)P(L)w^2 dA dL dx \tag{29}$$

where η denotes the new density function independent of pore length. Furthermore, they defined the growth rate function of a pore as:

$$\frac{dA}{dt} = \psi(A, x, T) \tag{30}$$

where ψ depends on the type of acid treatment.

Basically, two different mechanisms determine the growth rate. The first is the change due to reactions taking place, while the other is the merging of pores. Focusing on the pores within a certain area range implies that the number of pores within this group remains constant except those who enters and leaves by collisions. Defining the number of creations and destructions of pores as $\{\Delta\eta\}_C$ and $\{\Delta\eta\}_D$, respectively, the above statement yields:

$$\frac{\partial \eta}{\partial t} + \frac{\partial(\psi\eta)}{\partial A} - \{\Delta\eta\}_C + \{\Delta\eta\}_D = 0 \tag{31}$$

Furthermore, Schechter and Gidley defines both $\{\Delta\eta\}_c$ and $\{\Delta\eta\}_D$. By considering that a pore with area A_2 will grow and collide with pores with an area of A_1 and form pores with the area $A = A_1 + A_2$. The net creation can therefore be defined by the sum of all collisions of such a nature:

$$\{\Delta\eta\}_C = \bar{L} \int_0^A \psi(A_2, x, t)\, \eta(A - A_2, x, t)\eta(A_2, x, t) dA_2 \tag{32}$$

where $\overline{L}$ is the mean pore length. In the integral, the upper limit for A_2 is set to A since if one of the pores has an area larger than A the area of the created pore will become greater than A.

The rate of destruction is obtained by summing the number of collisions between pores with area A. Pores of size A can grow and meet A_2 and vice versa, though the result is the same, hence

$$\{\Delta\eta\}_D = \bar{L} \int_0^\infty [\psi(A, x, t) + \psi(A_2, x, t)]\eta(A_2, x, t)\eta(A, x, t) dA_2 \tag{33}$$

which implies an evolution of the pore size distribution due to a growth ψ given by:

$$\begin{aligned} \frac{\partial \eta}{\partial t} + \frac{\partial(\psi\eta)}{\partial A} = \bar{L} \Bigg\{ & \int_0^A \psi(A_2, x, t)\, \eta(A - A_2, x, t)\eta(A_2, x, t) dA_2 \\ & - \int_0^\infty [\psi(A, x, t) + \psi(A_2, x, t)]\eta(A_2, x, t)\eta(A, x, t) dA_2 \Bigg\} \end{aligned} \tag{34}$$

The latter equation is rather complex and solutions are difficult to obtain. In the presentation, two solutions are presented: the first being based on assuming no pore collisions and the second has the assumption that the rate of pore growth is proportional to the area. The derivation of their result is not reviewed here and we refer to the paper for more details.

Surface reaction within the pore structure is of greater interest and is much more relevant for the current report. In the further development of the pore growth expression, Schechter and Gidley investigate the surface reaction process within a specific pore. The following derivations are based on pore geometry as shown in Figure 5.

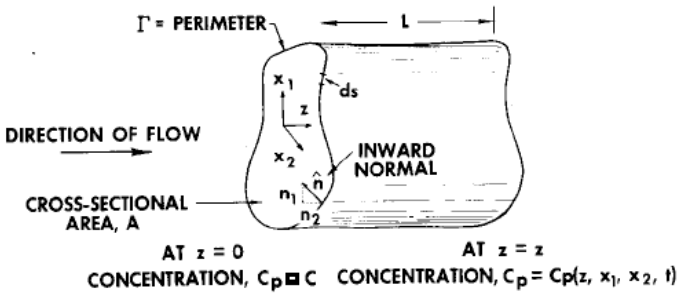

Figure 5: Idealized pore, showing coordinate systems for derivations. [7]

According to the above figure, the concentration C_p at position z and the point $\{x_1,x_2\}$ is given by $C_p(z,x_1,x_2,t)$. The concentration has to fulfill the following mass-balance equation:

$$\frac{\partial C_p}{\partial t} + v(x1, x2)\frac{\partial C_p}{\partial z} = D\left\{\frac{\partial^2 C_p}{\partial x_2^2} + \frac{\partial^2 C_p}{\partial x_1^2}\right\} \quad (35)$$

Note that the above equation assumes negligible diffusion along the axial direction. Relevant boundary and initial conditions:

Boundary condition 1: $C_p = C(x,t)$ at z = 0 (36)

Boundary condition 2: $-D\left\{\frac{\partial C_p}{\partial x_1}n_1 + \frac{\partial C_p}{\partial x_2}n_2\right\} = kC_p$ on Γ (37)

Initial condition: $C_p = 0$ for t = 0 (38)

k is here the kinetic constant for the reaction which is assumed first order as argued with experimental work done by Hendrickson et al. [13]

Defining an average concentration at each axial position, $\frac{1}{A}\int_A v\frac{\partial C_p}{\partial z}dA = \bar{v}\frac{\partial \overline{C_p}}{\partial z}$ and applying Green's theorem, the mass-balance can be written:

$$\frac{\partial \overline{C_p}}{\partial t} + \bar{v}\frac{\partial \overline{C_p}}{\partial z} = \frac{D}{A}\int_\Gamma \left\{\frac{\partial C_p}{\partial x_1}n_1 + \frac{\partial C_p}{\partial x_2}n_2\right\}ds = -\frac{1}{A}\int_\Gamma kC_p ds \quad (39)$$

Apart from the velocity approximation, one more approximation is required. Schechter and Gidley propose the approximation of a quantity, ratio of mean surface concentration to the mean bulk concentration, defined by:

$$\alpha = \frac{-\frac{1}{\Gamma}\int_\Gamma C_p ds}{\overline{C_p}} \quad (40)$$

This quantity is dependent on the pore geometry, D, and k, though independent of time and position. Equation (39) can be integrated, yielding:

$$\overline{C_p} = C(x, t - \frac{z}{\bar{v}})e^{-\frac{\alpha k \Gamma}{A\bar{v}}z} \qquad \text{for} \quad t > \frac{z}{\bar{v}} \tag{41}$$

Consider a time interval dt, in which a pore increases in size by the amount dA due to dissolution. With γ and defined as solid mass dissolved per gram reactant mass and ρ_s the solid density we get:

$$\rho_s dA = \gamma k dt \int_\Gamma C_p ds \tag{42}$$

Using the average rate of change in area, $\left(\frac{dA}{dt}\right)_{avg} = \frac{1}{L}\int_0^L \frac{dA}{dt} dL$, and combining the above equations with the assumption that C(x,t) does not vary significantly during the time step L/v, the rate of change in area can be expressed by:

$$\left(\frac{dA}{dt}\right)_{avg} = \frac{\alpha\gamma k C(x,t)\Gamma}{\rho_s L}\int_0^L e^{-\frac{\alpha k \Gamma}{A\bar{v}}z} dz \tag{43}$$

which by integration yields a final growth rate expression of:

$$\psi = C(x,t)\frac{\gamma A\bar{v}}{\rho_s L}\left[1 - e^{-\frac{\alpha k \Gamma L}{A\bar{v}}}\right] \tag{44}$$

As intuitively expected, from this description, the growth rate shows a linear relationship with the reactant concentration, and it also depends on the pore geometry (A, Γ, L), surface dissolution kinetics (k, γ), matrix density (ρ), the mean velocity (v), and finally the ratio of mean surface concentration to the mean bulk concentration (α). The latter factor requires the pore shape to be specified, however, Schechter and Gidley demonstrates in their publication that α is not particularly sensitive to the chosen shape. An important finding, which we have also observed in our current experiment, is that bigger pores will grow faster and that this is a self-amplifying effect due to the increase in flow rate resulting from less resistance for the flow in this particular pore.

Schechter and Gidley compare their approach of deriving the growth rate expression with some previous work done by Rowan [14]. His model provides the conceptual framework behind the mathematics in Schechter and Gidley's work. However, the approach lacks two very important key considerations for the derivation. The first point involves the diffusivity and surface reactivity not playing any role. The second point is the missing spatial and temporal changes in the pore size distribution. The latter implies that as acid reacts at the inlet it becomes buffered which results in less reactive acid further away from the point of injection. Rowan also proposes that larger pores grow faster than smaller, resulting in a self-amplifying pore growth. Schechter and Gidley suggest, based on experimental observations, that this is only partial true: above a certain size the growth rate reduces again. This terminal size defines the radius at which the diffusion no longer is fast enough compared to the axial velocity for a complete replacement of the buffered brine at the pore wall. The system is diffusion limited. Growth will continue, though with a constant rate.

An experiment is presented in the paper, in which the result clearly shows that bigger pores grow faster and that a few holes start to conduct most of the acid enhancing the growth. Finally, the experiment shows that one dominant hole has been formed. This hole is what's being referred to as a wormhole. Figure 6 shows the size of the biggest pore as a function of time. It is evident that the growth rate increases with time suggesting that the pore conducts an increasing fraction of the reactant. Schechter states that these results cannot be predicted with calculations based on the capillary model unless acid reactivity is considered in the analysis.

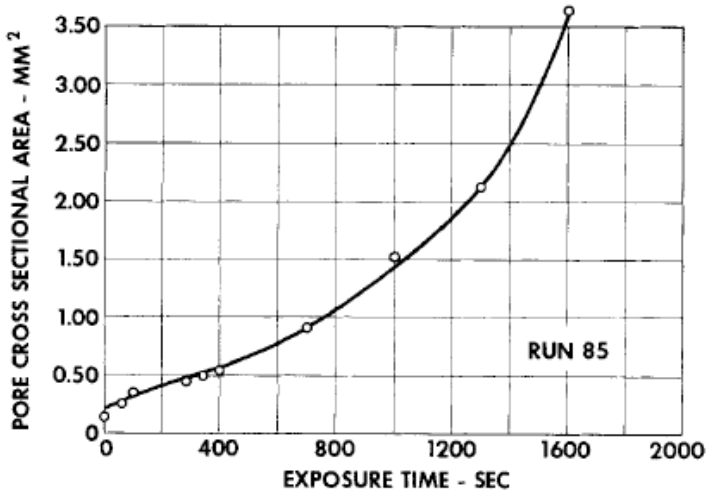

Figure 6: Pore size evolution with respect of time for the biggest pore.[7]

It is shown that the rate equation obtained earlier can be expressed as:

$$\psi = FXA^2\left[1 - e^{-\frac{18.1D}{FA^2}}\right] \tag{45}$$

where F = q/KLw^2 and X being the power of the acid (volume of dissolved solid/volume of spent acid). This expression enables some prediction of the wormhole behavior and suggests that: as the pore gets very large or in the case of having a strong acid power the growth rate will approach a constant value followed by a decline, which contradicts Rowan's [14] findings. This can easily be shown from equation (45): As the pore gets large ($FA^2/18.1D > 1$), then $\psi \rightarrow 18.1DX$. The growth continues, no longer with a rate proportional to the area squared. While the rate of growth for the cross section declines, growth rate in axial direction remains at the same level resulting in the formation of a wormhole. A diffusion-limited condition is achieved leaving the system in a convection dominant regime. This is what Schechter and Gidley propose in their paper as the explanation for the experimental observations and how wormholing occurs.

It follows in their publication an example at which the intent is to show that the idealized capillary approach derived earlier does predict this behavior of a wormhole. Schechter and Gidley present a calculation of the change in pore structure for one particular situation, at which the growth equation is modified accordingly, yielding equation (45). A detailed description of the calculation is presented in the paper, though not reviewed in this current report. The overall result however, is that the idealized model is able to predict the experimental observations to some extent. Thus as a final conclusion, Schechter and Gidley suggest that the model derived in their publication, is applicable to some extent for the prediction of wormhole

formation. The model describes the change in pore structure including the important growth rate factor ψ. Important findings are that pores of greater size grow faster and determine the systems response to acid.

A number of studies have shown that three distinct dissolution regimes are observed when carbonates are exposed to acidic brine, not only the wormholing regime focused on in Schechter and Gidley's study. It is also very important to know that precipitation of minerals can impair the permeability and other rock properties. Precipitation is not of any relevance for the experiment presented in this report and therefore not addressed in more detail. The current study concentrates mainly on the dissolution that follows from the interaction between the rock and acidic brine. As described in chapter 2, the mechanisms that govern reactive transport in rocks are advection, diffusion and chemical reaction. Each of the mechanisms is responsible for different types of dominant dissolution patterns in which compact dissolution, wormhole-type dissolution and uniform dissolution are the three frequently observed regimes.

It is by now very well accepted, due to a large number of studies, that compact dissolution (diffusion predominant) or wormhole-type dissolution (convection predominant) patterns are observed in a reaction controlled system, while uniform dissolution is expected to be seen in a transport-controlled system.

A compact dissolution pattern is recognized as a sharp dissolution front at the inlet followed by a more or less unaffected formation. Wormholes are channels penetrating the matrix. There are different types of wormholes, but the most common one is the branched type. Changes in properties are more localized in case of wormholing; however, they still might have severe impact on, e.g., the geomechanical strength of the rock. Figure 7 shows the different dissolution regimes both on a microscopic and macroscopic scale.

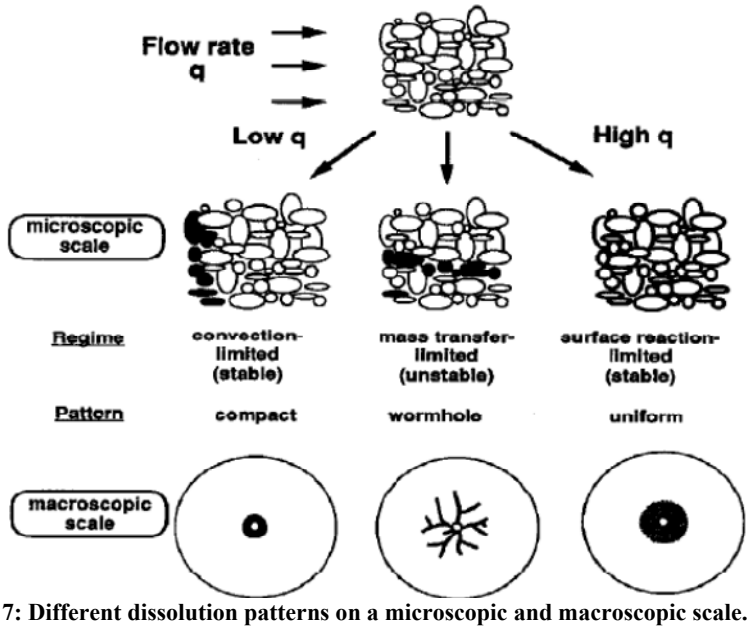

Figure 7: Different dissolution patterns on a microscopic and macroscopic scale. [15]

Uniform dissolution results in a more homogeneous leaching of the formation affecting more of the average properties of the formation. On field scale, these different dissolution patterns are observed in specific regions. The compact and wormhole-type dissolution are most frequently observed near the well bore, whereas uniform dissolution is more common in the far field region.

To understand and be able to model these dissolutions regimes has been an important topic for several decades. Mostly, the focus has been on wormholing its applicability in well bore stimulation. Wormholes have proven to reduce skin effects by penetrating the skin-affected zone and thereby enhance permeability. In a study on "Carbonate acidizing: toward a quantitative model of the wormholing phenomenon" Daccord et al. [16] showed that low rates cause a compact dissolution, meaning that most of the acid will be spent at the inlet, while intermediate rates results in wormholing. Finally, at high rates a more uniform dissolution is to be expected. A quantitative description of the dissolution regimes based on the Péclet number and the Peclet-Damköler number is one of the main results of their study. Before the work by Daccord et al. [16], which will be reviewed in the following part, little was known about matrix acidizing of carbonate reservoirs.

The objectives of their study were to obtain a better understanding of the evolution of wormholes and the analogy with dissolution pattern generated by using the model of diffusion-limited aggregation [15]. They wanted to show that the quantitative description of wormholes for a given geometry requires only one parameter and that their growth depends on the geometry of the system. Furthermore, they defined equations that describe the absolute penetration of the reactive fluid or in other words, the expected length of a wormhole, and applied them to model previous experimental results. As a conclusion, they aimed for a clear definition and a better understanding of the transition zones between the different dissolution patterns and finally investigated whether an optimum injection rate exists.

Their study and results is based on two approaches. The first one uses a series of experiments with two geometries, linear 1D and radial. All experiments involve injection of pure water at constant rates in limestone plaster samples. Different dimensions are studied where the diameter/length ratio is varied in the linear case and the axial length for the radial case.

Numerical simulations are used in the second approach, assuming a square grid of pores for which the radii are randomly chosen. Enlargement of the pores, as done in previous studies [17], is used for modeling the dissolution.

An important finding from the 1D case is that the pressure drop over the sample decreases linearly with respect to time. This is consistent with the formation of a wormhole of length, L_e, in which the pressure drop equals zero from the inlet and along this length, whereas Darcy's law applies for the remaining length, $L - L_e$.

$$p(t) = \frac{\mu q}{k\pi r_0^2}[L - L_e(t)] \tag{46}$$

r_0 is the radius of the sample. From this it follows that $L_e = L \cdot t/t_0$, where t_0 corresponds to the time of breakthrough. Daccord et al. define the dimensionless wormhole growth velocity, v_D, as v_{WH}/v_c, where v_{WH} is the actual wormhole velocity and v_c is the front velocity in case of total rock dissolution. By varying the fluid nature, injection rate and sample properties (permeability, porosity and solubility), they found that v_D is independent of the acid capacity number [18]. The acid capacity number is a quantification of the overall buffering capacity of the acid. However, v_D decreases with the flow rate according to $v_D \alpha q^{-1/3}$. Basically, the validity of this dependence is observed to hold between a lower and an upper limit:

At very low rates, complete buffering of the solution at the inlet is observed yielding a rather compact dissolution pattern which they refer to as compact dissolution. This pattern is seen during conditions yielding a Péclet-number less than unity.
At high flow rates, the pressure decrease response deviates from the linear behavior initially as well as yielding a discontinuity at the time of breakthrough. Daccord states that these deviations correspond to the distance between the tips of the wormhole and L_e [16], see Figure 9.

Daccord et al. also points out that both an increase in flow rate and a more homogeneous sample enhance uniform leaching, which is verified both by simulations with variations in the pore-size distribution as well as experiments, see Figure 8 below.

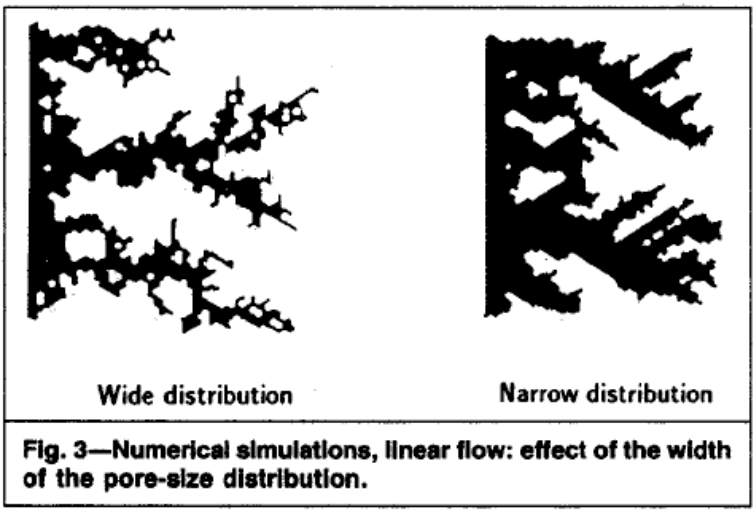

Figure 8: Effect of increasing the width of the pore-size distribution. [16]

An interesting result from the numerical simulations is that as the injection rate is increased, transitions between different dissolution patterns take place. A stable and compact dissolution pattern is observed for the lowest rate with the transition to more unstable and wormhole-like dissolution for intermediate rates, whereas for high rates, a transition to becoming more homogeneous dissolution is observed. These observations agree well with experimental findings. An increase in width of the acidizing channels is observed to yield a more homogeneous etching as well.

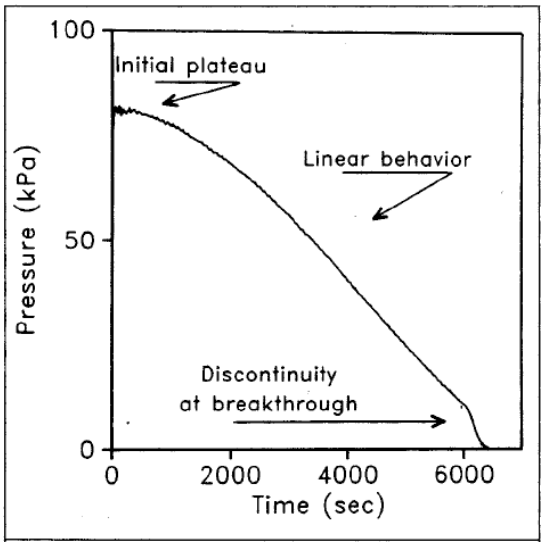

Figure 9: Pressure curve for linear 1D case[16]

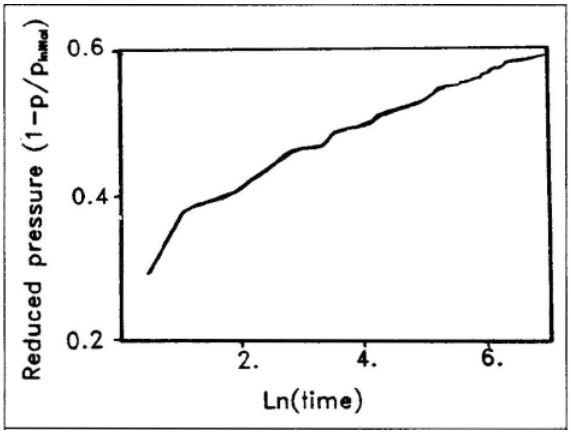

Figure 10: Reduced pressure cure for radial case in a semi-ln plot. [16]

They also find an expression for the wormhole length as a function of injected volume, V:

$$L_e(V) = \frac{\alpha V N_{ac}}{\pi r_0^2 \phi}\left(\frac{q}{D r_0}\right)^{-1/3} \tag{47}$$

where α is a dimensionless constant determined experimentally and N_{ac} is the acid capacity number.

The fundamental difference between linear case and radial case is that the equivalent radius, r_e, which corresponds to the penetration length L_e in the linear case, does not grow linearly with time. It is found that $r_e \propto t^{\alpha}$, with $\alpha=0.65\pm0.07$, which indicates a fractal behavior. This fractal behavior is not obtained in the linear case. Otherwise, the similarities with the linear case are clear: With the definition of a dimensionless wormhole velocity, similar to the one for the linear case, a dependence of $v_D \sim q^{-1/3}$ is found as well with a compact-wormhole transition zone around a Péclet number on the order of one. The numerical simulations are similar as well, with the exception of that the pressure behavior, which as expected from geometry, displays a logarithmic rather than linear time dependence (see Figure 10). The authors conclude that their results are consistent with the DLA (diffusion-limited aggregation) model [19], which implies that

$$v_D = b r_e^{(2-d_f)} Pe^{-1/3} \tag{48}$$

where b is a constant, r_e the radial penetration and Pe the Péclet number for a radial geometry. This yields a penetration for a given volume of fluid according to:

$$r_e(V) = \left[\frac{bVN_{ac}}{\pi h \phi}\left(\frac{q}{Dh}\right)^{-\frac{1}{3}}\right]^{1/d_f} \tag{49}$$

The equation above implicitly assumes injection along the axis meaning that the wellbore radius (r_{WB}) is neglected.

Now knowing the equivalent radius, the skin factor $s = (k_0/k - 1)\ln(r/r_{WB})$, which is equal to $-\ln(r_e/r_{WB})$ in case of no pressure drop over the distance r_e, can be expressed as:

$$s = \frac{1}{d_f} ln\left(\frac{bVN_{ac}}{\pi h \phi r_{WB}^{d_f}} Pe^{-\frac{1}{3}} + 1\right) \quad \textbf{(50)}$$

Certain conclusions can be made based on the observed results. Daccord et al. proposes:

1) the use of the equivalent length as a unique characterization of a wormhole would aid in generalizing the flow properties of the whole pattern making the knowledge of the exact number of wormholes obsolete, and
2) to represent the actual penetration rate with the dimensionless value v_D.

Daccord et al.'s findings regarding the estimation of penetration and well stimulation were verified by acid treatments carried out in a well. Furthermore, with regards of well treatment they were able to quantify the different dissolution regimes, and an optimum flow rate was suggested. Preferably, a Péclet number of 10, with gravity effects considered, should be used to avoid compact dissolution and achieve wormholing.

The results from this study had a significant impact on later studies. The ability to quantify the dissolution regime has been and still is quite beneficial and of great importance. Different mapping techniques have been proposed based on Daccord's [16] findings. Egermann, as described below is one of many that exploit Daccord's findings.

In addition to the Péclet number used by Daccord, later the Damköhler number has also been included as a parameter in the quantification of the dissolution regimes. Steefel and Maher [3] have published an extensive review on reactive transport. They summarize previous studies and definitions and give a nice overview of the different mechanisms, reactions, and equations. The section on the basics of reactive transport is of particular interest as it for a nice illustrates the impact of the Péclet and Damköhler numbers on the dissolution regimes.

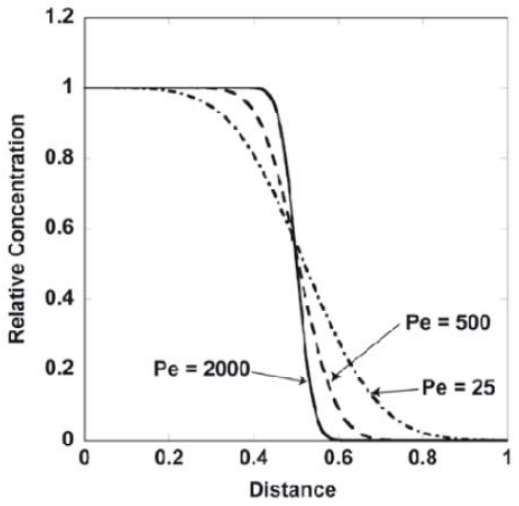

Figure 11: Effect of the Péclet number on the concentration profile at a certain point in time. The

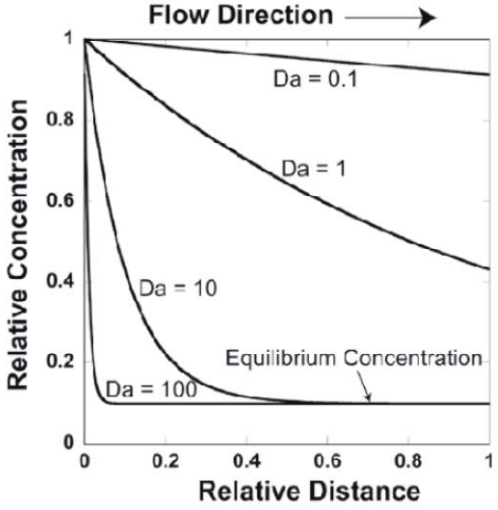

Figure 12: Effect of the Damköhler number (Da_{II})

system assumes negligible diffusion. Decreasing Péclet number means that diffusion gets more dominant allowing the fluid to disperse more into the matrix. [3]

on the concentration profile. This system assumes a very slow injection velocity. Higher Damköhler number means reaction predominance, thus a buffering closer to the inlet. [3]

They present a dimensionless form of the reaction equation (see equation (14)).

$$\frac{\partial C'}{\partial t'_D} = \frac{\partial^2 C'}{\partial x'^2} - Pe\frac{\partial C'}{\partial x'} - PeDa_I C' \tag{51}$$

Da_{II} is the Damköhler for diffusive transport, comparing the relative importance of the diffusive versus the advective transport. The equation makes it clear how the Péclet and Damköhler numbers control the behavior of the ADR - equation. In Figure 11 and Figure 12 the effect of the Péclet and Damköhler numbers on the concentration profile vs. distance is shown. Note that these pictures do not show the same system. For further reading, we refer to their publication.

One very well-known issue with laboratory experiments is that the conditions at which they are carried out results in either compact or wormhole-like etching patterns (Egermann et al. [20]; Grigg and Svec [21]; Svec and Grigg [22]). As a consequence, the uniform-dissolution regime is less well understood.

As mentioned earlier, in the field, compact and wormhole-type dissolution dominates the near well-bore region, whereas uniform leaching is more common in the far-field region. This latter dissolution regime is expected to result in a more homogeneous modification of the pore structure. Previous analysis of core samples and reservoir studies by, Mathis et al. [23], Kane [24], Kamath et al. [25], Christman and Gorell [26] and Prieditis et al. [27], have pointed out the consequences of CO_2 flooding in the far-field regions. The lack of studies on uniform dissolution was the main motivation for Egermann's [20] study on "An Integrated Approach to assess the petrophysical properties of rocks altered by rock/fluid interactions (CO_2 injection)", which will be reviewed in the following. The study aims to develop a procedure for homogeneous etching of core plugs, i.e. to stay in the uniform dissolution regime. To this end, Egermann et al. use Daccord's findings on the transition zones. To recap, the quantification can be made based on the dimensionless Péclet number (Pe) and Damköhler number (Da), see Figure 13. (Schechter and Gidley [7]; Daccord et al. [15]; Bekri et al. [28], [29])

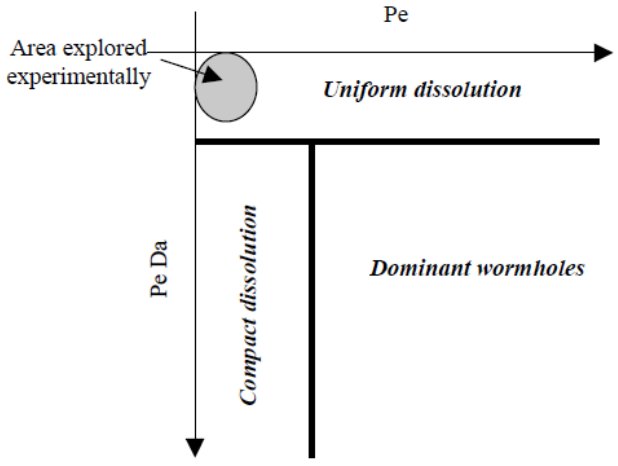

Figure 13: Dissolution regime as a function of Péclet and Damköhler numbers. [20]

The plot also shows the region at which Egermann aims to work in, which basically corresponds to Pe → 0.

The setup used is mainly composed of a core holder in which a sample with a typical size of 50 mm in diameter and 30 mm in length is mounted. This diameter-length ratio is important in order to ensure uniform placement of the acid within the sample. Furthermore, the core holder is attached to four different devices

- A nitrogen injection system for brine displacement.
- A brine injection system to remove reaction products.
- Vacuum on each side to prevent gas trapping.
- A buffer cell with 50% acid and 50% pressurized nitrogen.

A differential pressure transducer is used for measuring the permeability, a U-tube system based on gravity head differences is used as well. A certain back-pressure is adjusted by a Back Pressure Valve (BPV). The samples undergo a number of repeated cycles constituting of flooding, vacuum treatment, injection of acid from two sides, reaction, cleaning and displacement of products. Before and after the acid treatment a number of rock parameters are measured. Finally, the sample is dismounted and weight and porosity are measured, both before and after drying. One important assumption that is made is that the intermediate variations of the porosity are directly proportional to the treatment number since the same volume of acid is injected in each treatment.

Two limestone rock types were investigated, one with low permeability, 1.76 mD, and one with a higher permeability, 468 mD. The experimental results show clearly that the evolution of the permeability as a function of porosity increase is strongly dependent on the rock type with an enlargement of about 35% for the low-permeability rock and about 65% for the high-permeability rock for a porosity increase of 7%, see Figure 14.

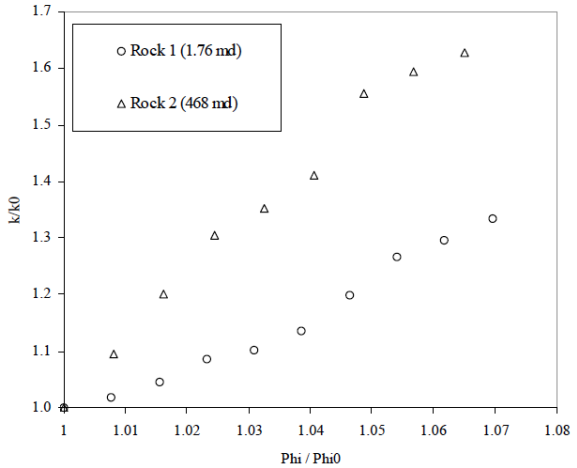

Figure 14: Evolution of the petrophysical properties (k / φ) for two different rock-types. [20]

The mercury porosimetry measurements, before and after the acid treatment are displayed in Figure 15. The mean hydrodynamic radii are also included. The mean hydrodynamic radius is the radius of the pores that conducts most of the fluid. The measurements show that the distribution of small pores is rather unaffected for both rock types. Egermann explains this result by the presence of irreducible water preventing acid from entering the smaller pores. For the low-permeability rock type,

the distribution of intermediate pores increases, whereas the large pores distribution decreases. The opposite trend was seen in the high-permeability rock type. In conclusion, pore structure is of significant importance for acid-induced rock alteration. The difference in the pore-structure alteration may explain the difference in permeability enlargement observed for the two rock types. Pronounced alteration of the biggest pores is seen in the second sample for which higher permeability enlargement is seen. Based on the results above, Egermann believes in good correlation between the proposed approach and CO_2 flooding processes in the field.

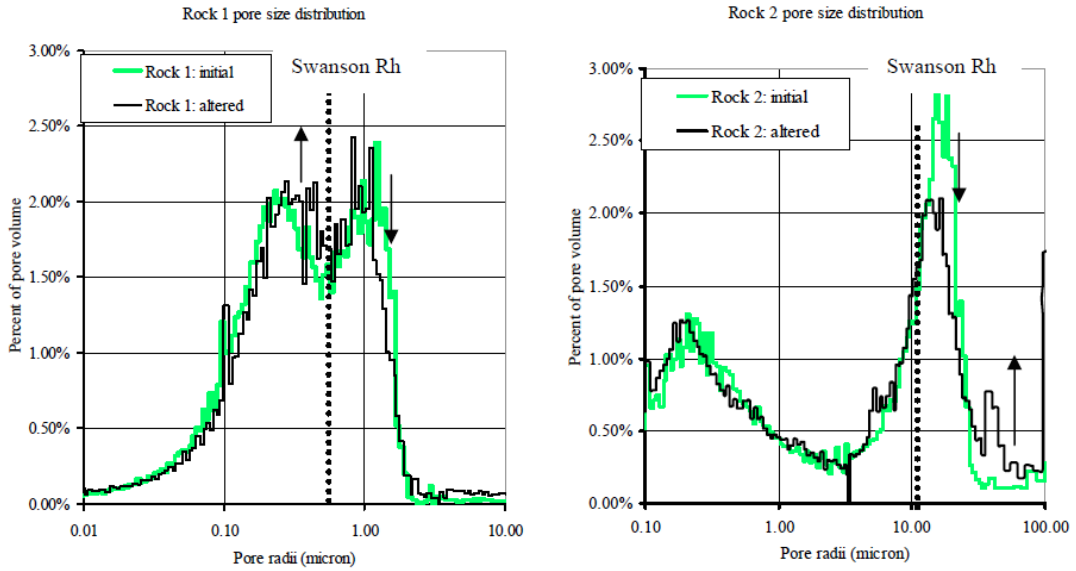

Figure 15: Results from the mercury porosimetry measurements. Left is prior to the experiment, right is after. [20]

In the second part of the study, a pore network approach is used in order to predict the changes in the petrophysical properties of the formation caused by the dissolution from CO_2 flooding. The goal is to match the modeling with the experimental results presented above. We refer to the appendix in Egermann's report [20], as well as the work by Laroche and Vizika [30] for a description of the applied model. The model is parameterized by properties obtained experimentally for the first rock sample used in the experimental part of the study. The pore-size distribution in the model is calibrated such that a match with the measured capillary pressure is obtained. The model is able to simulate the different dissolution regimes by:

- increasing pore-throat and pore-body uniformly for uniform dissolution,
- enlarging the pore-body for compact dissolution, and
- enlarging the pore-throat for wormholing.

Based on a combination of these methods, five different scenarios are:

- Reaction limited dissolution → pore-bodies and pore-throats uniformly increased, S1.
- Diffusion predominant dissolution regime → only increase in the pore-body radii, S2.
- Convection predominant dissolution regime → only increase in the pore-throat radii, S3.
- Reaction limited with pore-body growth twice as fast as the throats, S4.

- Reaction limited with pore-bodies and throats grow proportionally to their radii, S5.

As was addressed in the first part of this literature study Schechter and Gidley [7] concluded that large pores grow faster, which is represented by the two last scenarios, S4 and S5. The amplitude of the dissolution is represented by a thickness τ. The simulations are carried out by calculating the changes in permeability and porosity at different values of τ. The results can be seen in Figure 16, which also includes the experimental data obtained for the first sample. It is evident that scenario S4 yields the best match and corresponds with the experimental results.

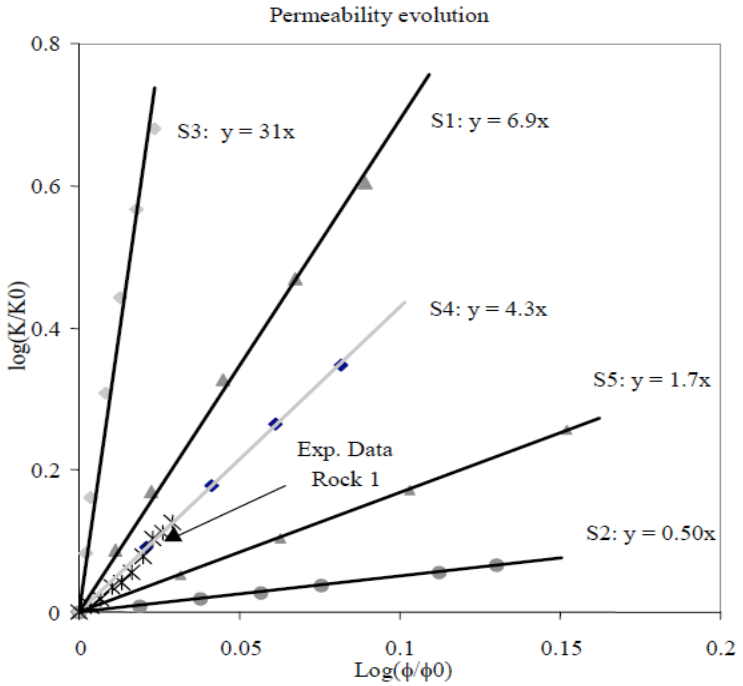

Figure 16: Evolution of the permeability vs. the normalized porosity using the different dissolution scenaria (the experimental dissolution results are represented by crosses). [20]

Egermann concludes with that the proposed experimental approach is a reasonable method for uniform dissolution. Furthermore, comparing experimental data with pore network simulations is suitable for identifying the dissolution mechanism, and to provide quantitative information about petrophysical properties.

4 The Experiment

4.1 Core type and initial properties

The core sample used in the experiment was a dry drilled sample from the Euville Outcrop located in the northern part of France. The mineralogy for the sample is rather simple, consisting mainly of calcite ($CaCO_3$) with some clay minerals (~ 2%).

Petrophysical and hydrodynamic properties such as porosity, permeability, density, lithology etc. were obtained by standard core analysis, including pressure mercury injection and gas permeability measurements yielding porosity, surface area per unit pore volume and threshold pressure. The sample is characterized by having a beige color with quite qualitative sized angular grains.

Also, physical dimensions such as length, diameter and weight were measured which is summarized in Table 2 together with the other pre-test petrophysical properties. In addition to the core analysis, CT scanning was performed. For the CT-scanning a total of 74 scans along the length of the core resulting in cross sectional images were obtained. PanTerra performed the high-pressure mercury injection to extract the pore size distribution.

Table 2: Initial properties of the Euville core sample used in the experiment.

Property	Value	
Length	76.16	*mm*
Diameter	37.83	*mm*
Weight	194.88	*gram*
Grain density	2.68	g/cm^3
Bulk volume	85.60	*ml*
Pore volume	12.84	*ml*
Porosity	0.15	
Surface area of grains (per pore volume unit)	20.42	m^2/cm^3
Permeability	80	*mD*

4.2 Experimental setup

A schematic setup of the experiment is shown in Figure 17. It includes an autoclave containing the brine, which also featured a stirring mechanism for mixing CO_2 and brine. A bottle with 60 bar CO_2 pressure was attached to the autoclave. The autoclave was connected to a Quizix pump (pump 1) used for pumping CO_2-saturated brine through the core plug. There was also an ISCO pump connected to the compaction cell, which was used for brine flow prior to the CO_2 flooding. Both the Quizix and ISCO pumps feature the ability to deliver fluid at constant rates and high pressures. With the Quizix pump is better suited for smaller volumes, the ISCO has a slightly smaller flow-rate, but a higher capacity.

The cell that the core sample was built into was a triaxial compression cell. Figure 18 shows a schematic drawing of the cell. The sample was placed between titanium end-caps and enclosed in impermeable Teflon Shrink tubing and a 2.5 mm thick HNBR sleeve. The end caps featured bores to enable fluid access. The

pressure vessel in which the assembly was placed in had a capacity of 100 MPa axial and radial pressure. To achieve axial loading, a hydraulic piston, driven by fluid pressure, was placed in the chamber at the bottom of the piston in which pressure was obtained by fluid pressurizing. Axial pressure was measured using a 100 MPa pressure gauge. Radial stress was applied by pressurizing the oil that surrounded the elastomer sleeve. Pore fluid pressure was applied through the top end-cap and monitored both at the top and bottom with a 100 MPa gauge. This allowed for verification of full pore pressure communication during the experiment.

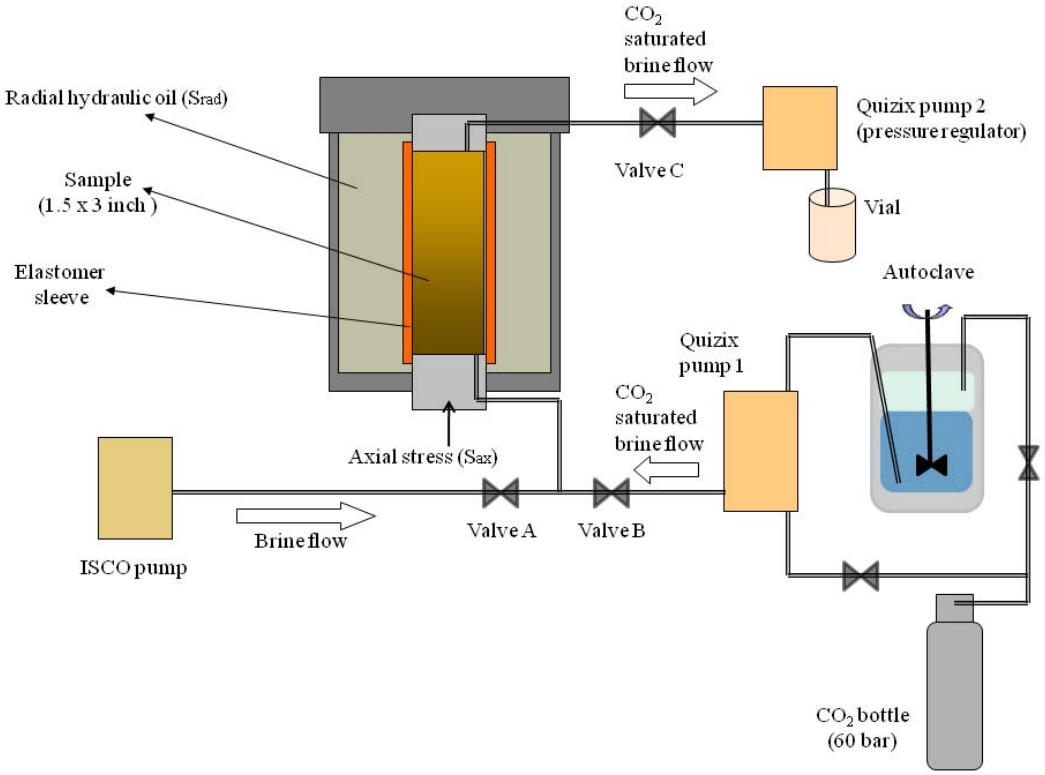

Figure 17: Schematic of the experimental setup.

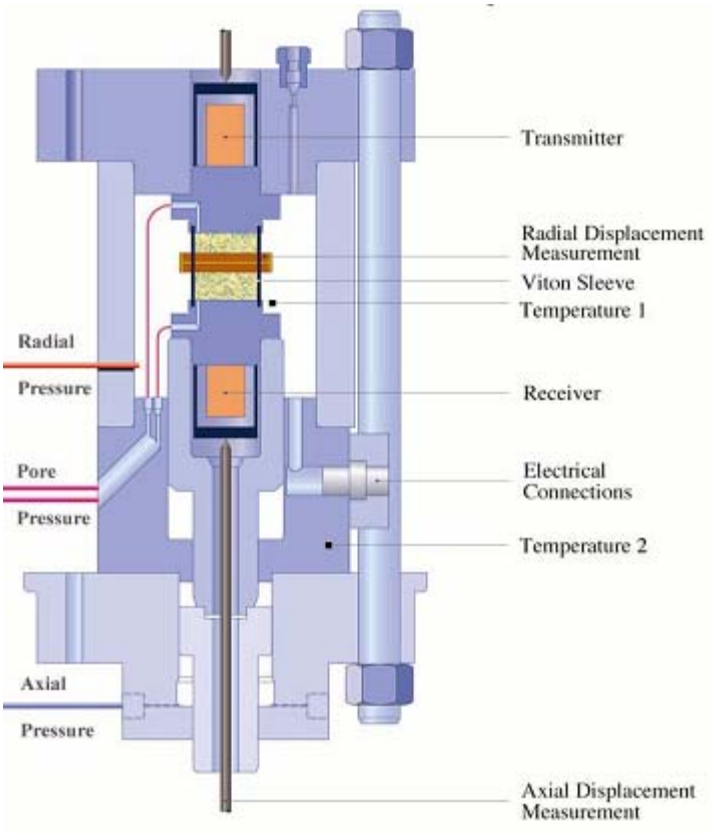

Figure 18: Schematic drawing of the compression cell.

The compression cell also featured two linear variable displacement transducers for continuously measuring the sample length. Note that the axial deformation of the titanium end-caps due to axial load and temperature was accounted and corrected for. Diameter measurements were made by clamping a cantilever bridge equipped with foil strain gauges onto two pins penetrating the sleeve and being in direct contact with the sample. Piezoelectric transmitter and receiver were integrated in the end caps for ultrasonic velocity measurements in axial direction; a radial transducer set-up was used for the radial velocity measurements. A second Quizix pump was connected to the outlet of the cell. It was used to maintain a certain back-pressure in the flow loop. A 10 ml sampler was placed at the outlet of the pump to collect the effluent for further analysis. Data acquisition and experimental sequence control was done by custom-built software.

4.3 Procedure

The core sample was built into the cell without any pre cleaning. Both axial and radial stress was then applied to the core before the sample was vacuumed for approximately one hour. A fully saturated core was achieved by injecting brine into the sample.

The axial and radial stresses, as well as the pore pressure were then gradually increased to 257, 198 and 143 bars respectively over a period of 22 hours. Pressure level, axial and radial displacement and ultrasonic velocities were continuously monitored during this pressurization phase, with data points taken every 1 – 2 minute, (15 – 30 minutes for the velocities). Subsequently, the core was flooded with brine by the means of an ISCO pump to induce continuous brine flow for 27 hours with a total of 7 pore volumes. This was done in order to remove contaminations, impurities and

loose material in the core and the system of pipes and tubes and to make sure that any effects observed during subsequent flow of CO_2-saturated brine are due to the CO_2. The brine used throughout the experiment was mainly non-deionized tap water, thus some small amounts of impurities were present.

In the next step, CO_2-saturated brine was flowed through the sample. The saturation process of the brine took place in the 300ml autoclave in which a CO_2 pressure of 75 bars was induced at a temperature condition of 35 ^{0}C. This is the partial pressure in the autoclave after heating from room temperature. In Figure 17 the CO_2 bottle is labeled 60 bars, which is the pressure in the bottle at room temperature. Conditions, which the brine was exposed to after leaving the autoclave, were chosen in such a way that no CO_2 would come out of solution. The Quizix pump was fed with the brine, which pumped at constant flow rate. The CO_2 saturated flow stage was started 49 hours into the experiment. Different injection rates, which is listed in Table 3, where used throughout the experiment. In order to allow the experiment to run without supervision during weekends without having to refill the autoclave, injection rates were reduced. Total stresses and pore pressure were kept constant throughout the experiment (except for an unintended drop in pore-pressure at the beginning). The second Quizix pump ensured a constant back-pressure. The experiment was performed at room temperature (21 ^{0}C). Flooding was paused after 237 hours for creep behavior studies before being resumed and ending with a total of 125 injected pore volumes of CO_2 saturated brine. Four axial unload/load cycles were performed during this stage to determine rock mechanical parameters such as Young's modulus, Poisson's ratio and bulk modulus. Termination of the experiment occurred after 600 hours due to sleeve failure.

Table 3: Injection rates used in the experiment.

Flow rate #	Rate *[ml/min]*
1	0.06
2	0.12
3	0.20
4	0.025
5	0.035
6	0.1
7	0.08
8	0.0175

In addition to the pressure, displacement and ultrasonic velocities, pH of the effluent was frequently measured during the flooding. Length and diameter of the sample were also monitored continuously. Effluent analysis regarding Ca^{2+} concentration was approximately done every 30 injected pore volumes. The effluent experiences great depressurization as it leaves the system, resulting in a reduced solubility and precipitation of calcite. This is also evident by the results that are presented later, showing a much higher concentration in the effluent than what the solubility constant at standard condition yields for the expected solubility. In order to account for all calcite in the effluent prior to depressurization, the precipitated calcite was dissolved by acid prior to the measurement of the calcium content.

After the termination of the experiment, the core was dried and again placed in the CT-scanner and another set of 74 scans was taken along the length of the core. Post-test sample dimensions and permeability was measured as well.

5 Experimental results

Apart from the continuous measurements that were done for diameter, length, ultrasonic velocities and strains (which is not the subject of the present project), a total of 23 effluent samples were taken during the CO_2 flooding. The effluent was analyzed for calcium concentration four times during the flooding, not including the initial one. Table 4 summarizes these measurements. The post-test dimensions of the core are presented in Table 5. It is found that both the diameter and the length reduction were more or less negligible with values of respectively 0.05% and 0.29%. The reduction in weight is more significant and was found to be 2.85%. Note that this is the total change including possible changes during the pure brine flooding stage. pH and measured Calcium concentration as a function of cumulative injection are plotted in Figure 19 together with the respective average value.

Table 4: Measured calcium concentration and pH in the effluent during the experiment.

Cumulative CO_2 saturated brine injection	**#PV**	**$[Ca^{2+}]$**	**$[Ca^{2+}]$**	**pH**
[ml]		*[mg/l]*	*[mol/l]*	
0	0	3.399	0.000	7.15
402.0	31	1325.56	0.032	6.04
863.3	67	1385.76	0.034	6.10
1055.2	82	1232.62	0.030	6.14
1398.4	109	1082.07	0.026	6.14

Table 5: Dimensions of the core sample after the experiment.

Dimension	**Pre – test**	**Post – test**	**Change**
Diameter *[mm]*	37.83	37.81	0.02
Length *[mm]*	76.16	75.94	0.22
Weight *[gram]*	194.88	189.33	5.548
Permeability *[Darcy]*	0.080	12.95	12.87

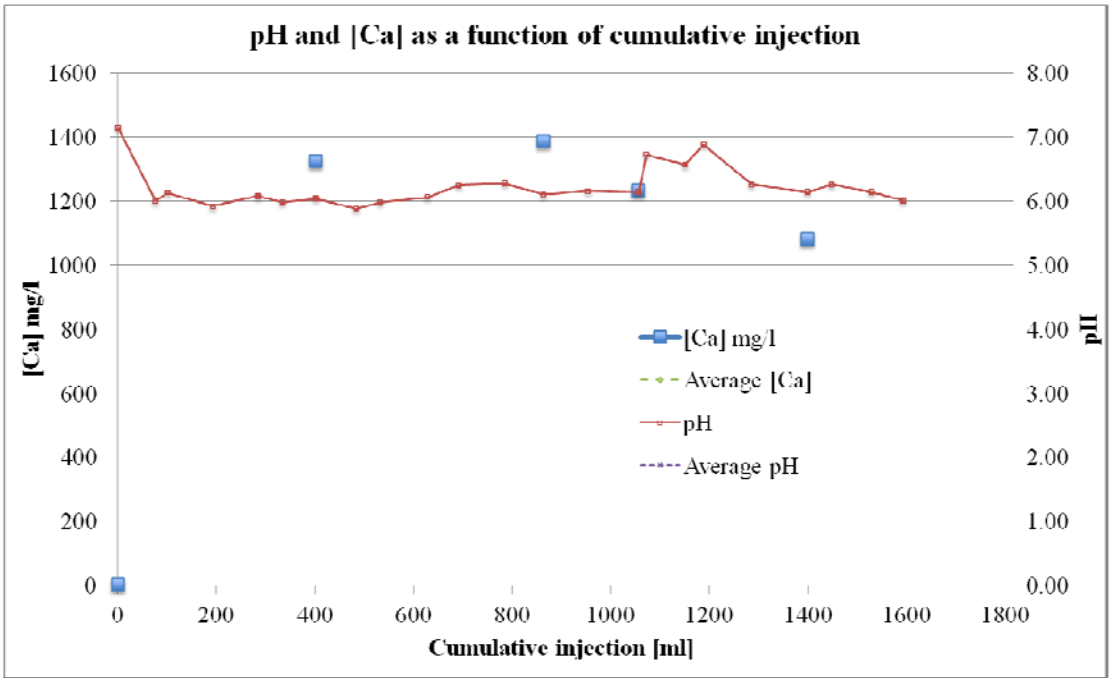

Figure 19: Calcium concentration, pH and the respective average values with respect of cumulative injection.

Overall, the average values amounted to $[Ca^{2+}]$ = 1260±130 mg/l or $[Ca^{2+}]$ = 0.031±0.003 mol/l and pH=6.20±0.3. The concentration of calcium and the stoichiometric relation between dissolved calcite and calcium concentration implies calcite dissolution of 0.031±0.003 mol/l which yields 3.06 g/l. Based on a total cumulative injection of 1617.5 ml the total amount of dissolved calcite is approximately 5.0 grams. As Table 5 shows, the weight reduction and thus the amount of removed material from the sample is 5.5 grams in which calcite results in making up 89% of it. There was also a significant increase in the permeability by 12.87 Darcy.

The four unload/load cycles resulted in estimations of the rock mechanical properties Young's modulus, Possion's ratio, bulk modulus and the shear strength. These test where taken independently of the effluent analysis. Due to the main objective for this project, these results are only briefly mentioned and presented. Figure 20, Figure 21 and Figure 22 show the variation in each of these properties as a function of the injected volume of CO_2-saturated brine.

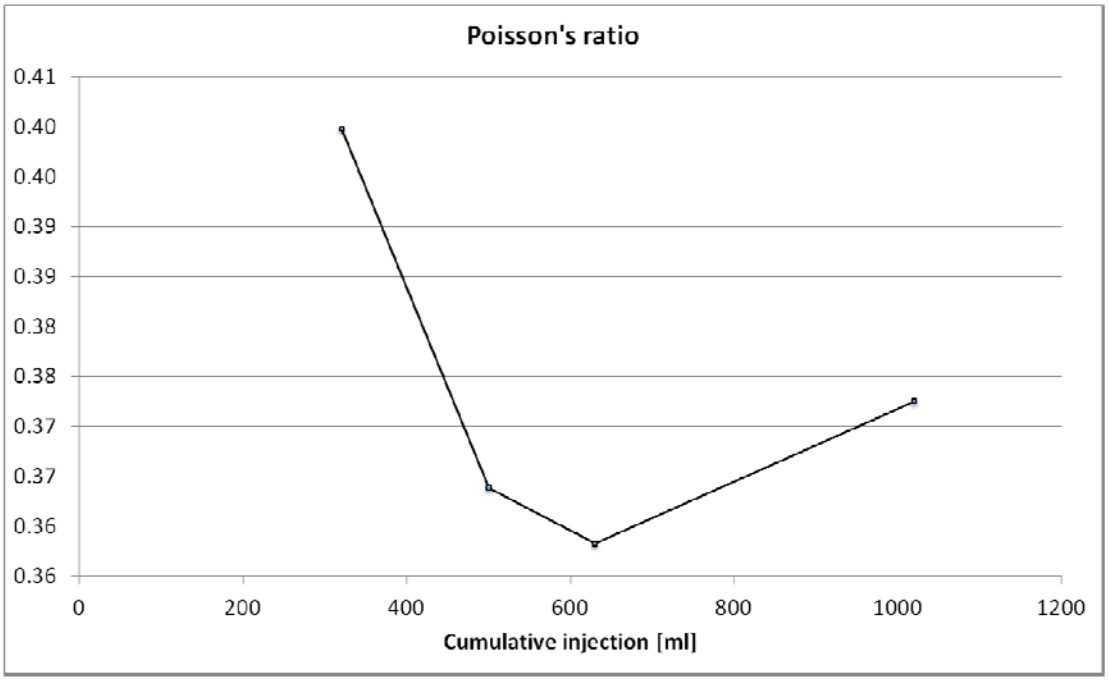

Figure 20: Variation in Poisson's ratio with respect of cumulative injection.

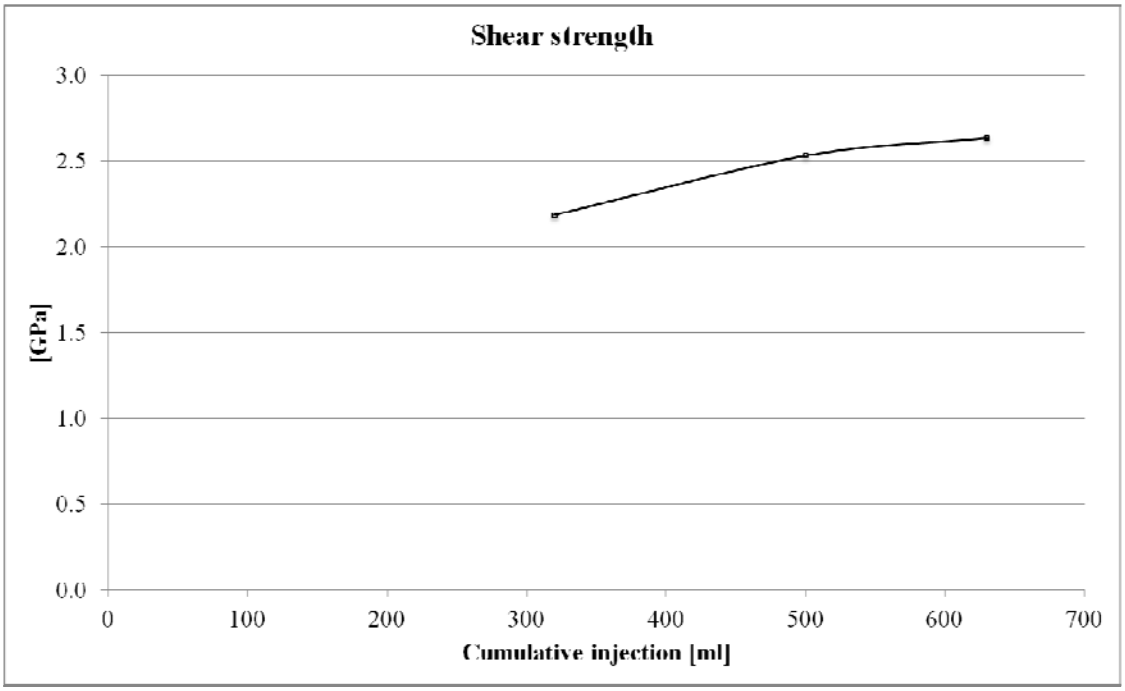

Figure 21: Variation in shear strength with respect of cumulative injection.

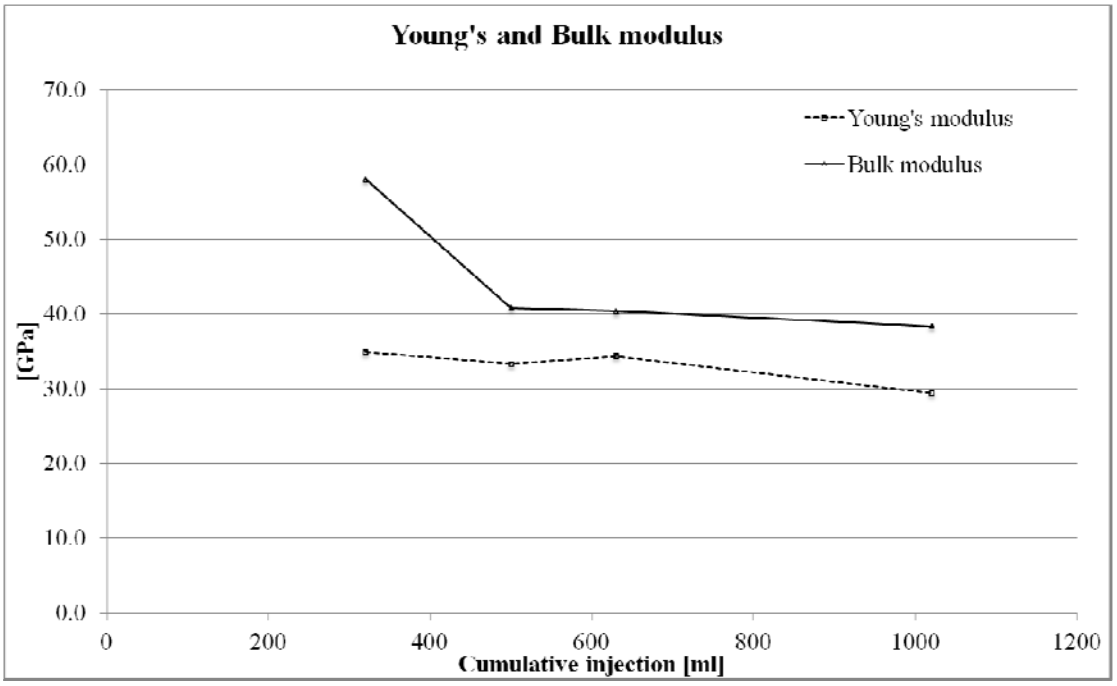

Figure 22: Variation in Young's modulus and the Bulk modulus with respect of cumulative injection.

6 Data visualization, analysis and discussion

6.1 Visual and CT-scan observations

By visual inspection of the core, we clearly see that approximately the two first millimeters from the inlet are strongly etched, while the rest looks rather unaffected. This might indicate that a compact dissolution regime was present in the core sample during the experiment. However, CT-scans show that a dominant wormhole of significant size has formed throughout the whole length of the sample (see Figure 23). The 3D picture (see Figure 24) of the core, in which the pore space has been filled and the grains are removed, illustrates the structure of the wormhole. Thus, it is already evident that the dissolution process was reaction-controlled. Determination of the dissolution regime causing the pattern seen at the inlet is more difficult and will be addressed further below. The presence of a reaction-controlled process is consistent with what previous studies have shown [20], [21], [22], namely that most laboratory experiments are conducted at conditions resulting in a compact or wormhole-type dissolution.

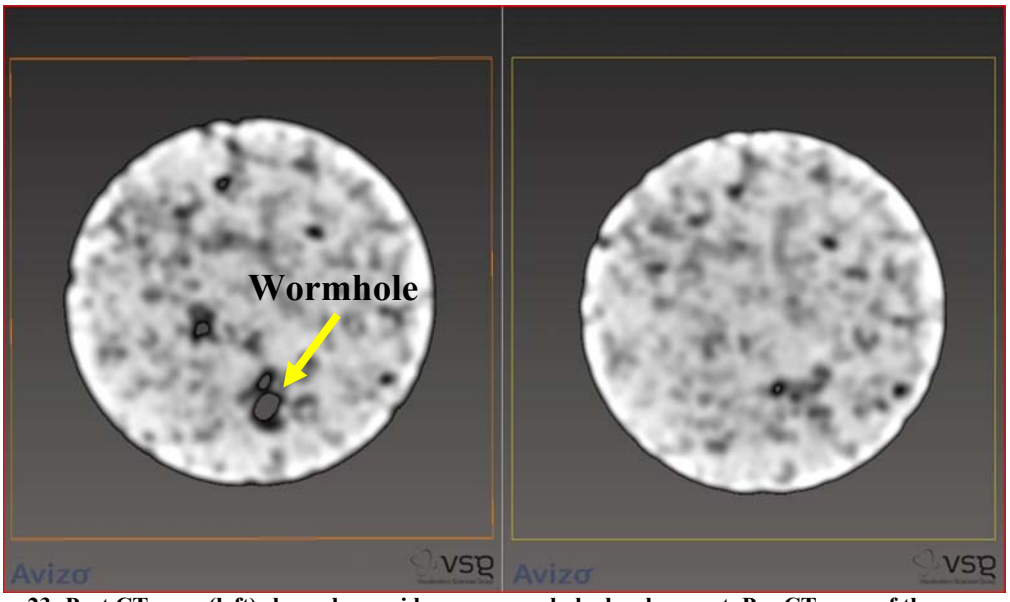

Figure 23: Post CT-scan (left) show clear evidence a wormhole development. Pre CT-scan of the same cross section is displayed to the right.

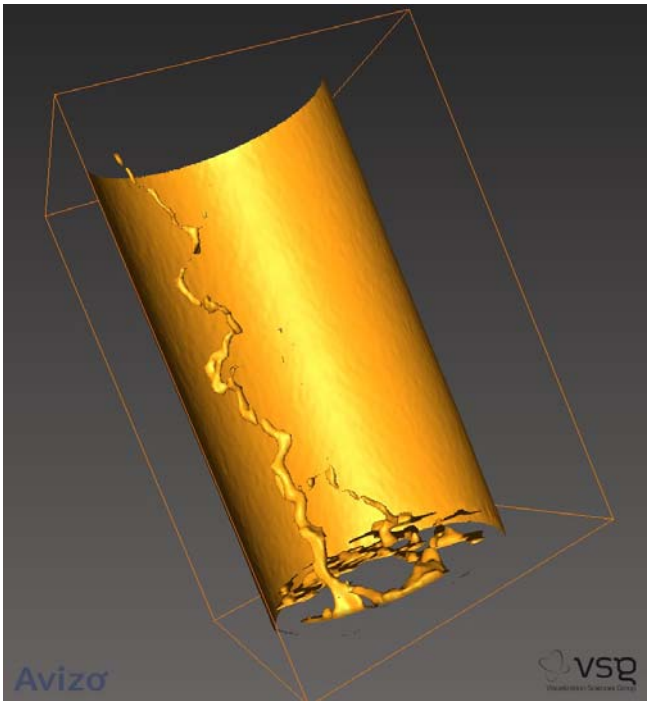

Figure 24: 3D image showing the wormhole developed throughout the length of the core sample. This picture was made by Fons Marcelis using Avizo.

6.2 Numerical estimation of dissolved calcite

Due to complexity of the chemical reactions involved in the dissolution of calcite and uncertainties of the rates and equilibrium constants, an accurate estimate is deemed difficult to obtain. A simplistic model has been developed in the frame of this study, which is used to estimate the solubility of calcite in CO_2-saturated brine. Since we believe that the dissolution process is reaction-controlled the solubility of calcite allows us to estimate the amount of dissolved calcite per injected pore volume of CO_2-saturated brine. By the use of Wolfram Mathematica 8.0, a program has been written that solves the system of equations listed in the theory section (equation (5), (6), (8), (10), (11), and (12)). The input parameters for the program are the dissociation constants, activity coefficients and since it is a closed system, initial CO_2 concentration in the brine. Note that the program gives the results in concentration, though the activities are accounted for through the including activity coefficients. The case of having an open system is also programmed, and both codes can be found in the appendix.

For simplicity, we assume in the present calculations that the activity coefficients equal to 1. Later, we will discuss the effect of activity coefficients smaller than 1. Objective was to see whether the program is able to predict the experimental results. The dissociation constants are estimated from the equations presented in the theory section (equation (21), (22) and (23)), for the condition (pressure and temperature) the experiment has been carried out with, and the initial CO_2 concentration, which is the expected amount dissolved during mixing in the autoclave, is found from the CO_2 solubility graph in the same section. Table 6 lists the different input parameters, and the results are shown in Table 7 for both a closed and open system.

Table 6: Input parameters for the numerical simulation of the solubility for calcite.

Input parameter	Value
K_1 (T=65 ^{0}C)	5.13×10^{-7}
K (T=65 ^{0}C)	24.27
K_w (T=65 ^{0}C)	1.2589×10^{-13}
$CO_{2,i}$ (P=75 bar, T=35^{0}C)	1.22 *[mol/l]*
K_H (only open system)	60.88

Table 7: Estimated solubility for calcite with various activity coefficients in a closed system and for the general case in an open system.

CLOSED SYSTEM						
γ	Ca^{2+} *[mol/l]*	H^+ *[mol/l]*	HCO^{3-} *[mol/l]*	CO_2 *[mol/l]*	OH^- *[mol/l]*	pH
1.0	0.0155	1.99×10^{-5}	0.0311	1.204	6.33×10^{-9}	4.70
OPEN SYSTEM						
γ	Ca^{2+} *[mol/l]*	H^+ *[mol/l]*	HCO^{3-} *[mol/l]*	CO_2 *[mol/l]*	OH^- *[mol/l]*	pH
1.0	0.0153	1.93×10^{-5}	0.0306	1.150	6.53×10^{-9}	4.71
EXPERIMENT						
γ	Ca^{2+} *[mol/l]*	H^+ *[mol/l]*	HCO^{3-} *[mol/l]*	CO_2 *[mol/l]*	OH^- *[mol/l]*	pH
1.0	0.0310					

First observation is that there is hardly any difference from an open to a closed system; the CO_2 concentration of the closed system is analytically larger that of an open system where it is kept constant by the presence of a gas phase with constant partial pressure. However, the estimated value for the calcium concentration is significantly lower than the experimental measured concentration in the effluent. There would be several reasons for the discrepancy:

(i) Uncertainties in the dissociation constants. We have not taken pressure dependence into account: however the uncertainties in the dissociation coefficients can probably only partly account for the discrepancy since relatively large parameter changes would be needed to result in a calcite concentration as measured in the experiment. This is illustrated in Figure 25 where we plotted the calcium concentration as a function of K_1.

(ii) We have assumed activity coefficients equal to 1. In reality, activity coefficients can be significantly smaller than 1, and they are also affected by the presence of other components such as salts. Numerical simulations are also done with different activity coefficients. For simplicity, activity coefficients are assumed equal for all species. The calcium concentration as a function of activity coefficient is shown in Figure 26. It is evident from Figure 26 that the activity has a significant impact. The activity coefficient must however be reduced quite significantly in order for a matching numerical simulation and experimental result.

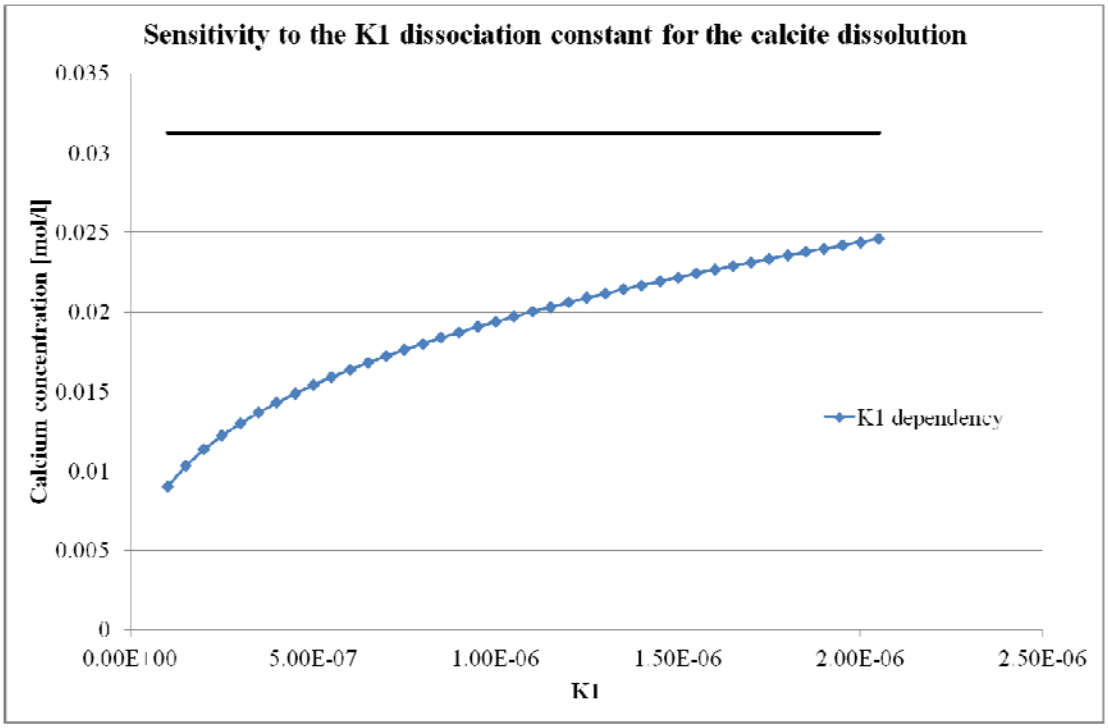

Figure 25: Sensitivity of the calcite solubility to the K_1 dissociation constant.

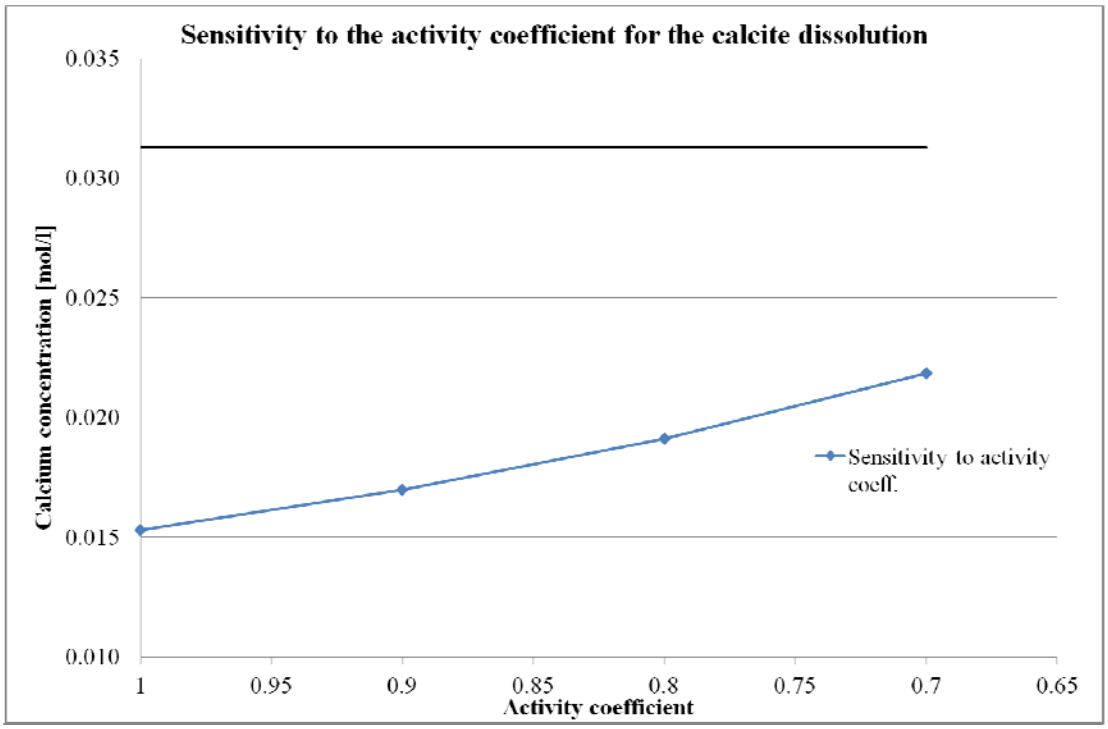

Figure 26: Sensitivity of the calcite solubility with respect to the activity coefficients.

It should be noted that there are also a number of possible error sources in the experiment. For example, non-deionized water was used resulting in the presence of impurities. These can disturb the chemical equilibrium, thus affecting the dissolution by either increasing or decreasing the solubility. From the experimental results, we also see that there is a difference between the total mass of material removed, and the dissolved amount of calcite. As the effluent leaves the core, it has to flow through pipes and a pump before reaching the sampler. While the pressure condition is

maintained up to the sampler, the temperature decreases on its way to the sampler, which might result in precipitation of calcite within the pipes. This would imply that the measured calcium concentration in the effluent is lower than the actual amount of Ca^{2+} leaving the core. Thus, the difference with respect to calculations might even be higher.

6.3 Determining dissolution patterns by the Péclet number

The transition zone between compact and wormhole-type dissolution is expected to be around a Péclet number of 1; smaller numbers yield compact, greater numbers result in wormhole formation. In order for the calculation of the Péclet number we need the diffusivity coefficient. This can be calculated by Einstein-Stokes equation:

$$D = \frac{k_B T}{6\pi\eta r} \tag{52}$$

Here, the k_B is Boltzmann's constant, T the temperature in Kelvin, η is the viscosity of the fluid that the particle of interest is dissolved in while r is the radius of the spherical particle of interest, which in this case is the radius of the Ca^{2+} molecules. Applying this yields a diffusivity constant equal to $D=2\sim3x10^{-9}$ [m^2/s]. Equation (18) is then applied with the sample length as the characteristic length, giving the respective Péclet number for each flow rate presented in Table 8.

Table 8: Calculated Péclet number for each of the applied injection rates.

Flow rate *[m/s]*	Péclet
8.90E-07	24.83
1.78E-06	49.66
2.97E-06	82.26
3.71E-07	10.35
5.19E-07	14.48
1.48E-06	41.29
1.19E-06	33.20
2.59E-07	7.23

All the flow rates yield a Péclet number greater than 1, which strongly suggests that wormholing is the dominant regime throughout the whole experiment. In the present experiment, the injection is spread over the cross section of the inlet, hence a dispersed injection. No compact dissolution regime implies that the inlet pattern consists of several wormholes due to the dispersed injection. These findings indicate that the convectional flow regime was predominant.

A high calcium concentration (higher than expected for a fully buffered solution according to our simple calculations) and a more or less constant value throughout the experiment, indicates that the brine is fully buffered (maximum calcium concentration) by the time it leaves the sample. A buffered effluent supports the assumption of having a reaction-controlled system. Figure 19 also shows, however, a small decrease in the calcium concentration after the injection of about 1400 ml CO_2-saturated brine. From this point on, the effluent is no longer buffered, implying that the system has shifted to a transport-controlled regime.

According to previous studies, a uniform dissolution pattern is expected when transport is the controlling mode. The transition from reaction controlled to transport controlled mode should in theory yield uniform dissolution. However, it is evident that apart from the wormhole, both visual examination and the CT-scans suggest an unaltered core sample elsewhere. A dominant wormhole will conduct most of the fluid [16] leaving the rest of the sample unexposed to the acidic brine, thus no dissolution elsewhere. The absence of uniform dissolution is therefore not surprising.

6.4 Formation of one dominant wormhole

It is obvious that wormholing is the dominant dissolution regime in the experiment. The formation of one dominant wormhole corresponds to the results from Schechter and Gidley's study [7]. Larger pores grow faster, resulting in enhanced permeability and the conduction of a higher fraction of the solution, which again enhances the growth in this pore. This is a self-amplifying effect. Dispersed injection at the inlet might explains the presence of several wormholes at the inlet. In the end, over a relatively short distance of only a few mm, the wormholes merges and only one wormhole continues to grow through the sample. It is like a competition, and the "strongest candidate" wins. Details of the wormhole structure are related to the pore structure of the sample and its heterogeneity on the pore scale. As Schechter and Gidley stated, the pore will reach a terminal size at which the growth rate of the cross sectional area declines, but maintaining axial propagation. The system is still in a reaction-controlled mode, resulting in a buffered effluent. Eventually, breakthrough of the wormhole will occur and the terminal size will shortly be reached along the whole wormhole. The system will at this point shift from reaction-controlled to transport-controlled mode, and also the effluent will no longer be buffered. Intuitively, this is a reasonable explanation for the experimental results, and it is consistent with Schechter and Gidley's study [7]. From the reactive-flow equation, we also see that the surface area of the grains is of significance. Leaching may result in a reduction of the surface area. This would lead to a decrease in the reaction rate and possibly contribute to transition from reaction to transport control.

Reaching terminal size does not imply zero growth. The terminal size is defined as the size at which the growth rate does not increase any longer. By examining the CT-scans, we can clearly see that the last part of the wormhole has a smaller cross section than the rest. The terminal size is, after all, reached last at the outlet.
From Figure 19 we see that the transition from reaction-controlled to transport-controlled is made almost at the very end of the experiment, thus the area of the wormhole at the outlet is a reasonable approximation for the terminal cross section area. This will be addressed later.

As mentioned above, the shape is similar to a cone, but far from what one should expect if the self-amplifying effect would continue with time. Schechter and Gidley explain this behavior in their study and show by examining equation (45). We should be able to explain the evolution of the wormhole and the shape it takes to some extent by also examining the general growth rate equation that Schechter and Gidley derives (Eq. 44). The following approach is similar to the one that Schechter and Gidley do on equation (45). Two extreme scenarios can be defined:

1. The exponent $\frac{\alpha k \Gamma L}{A\bar{v}}$ is large, i.e.:

$$\psi = C(x,t)\frac{\gamma A\bar{v}}{\rho_s L}\left[1 - e^{-\frac{\alpha k \Gamma L}{A\bar{v}}}\right] \approx C(x,t)\frac{\gamma A\bar{v}}{\rho_s L} \quad (53)$$

In this case, the growth rate depends on the cross-section area and thus the growth is proportional to r^2 ($A \propto r^2$), r being the radius of the wormhole cross-section.

2. The exponent is small and the exponential term can be expanded in a Taylor series:

$$\psi = C(x,t)\frac{\gamma A\bar{v}}{\rho_s L}\left[1 - e^{-\frac{\alpha k \Gamma L}{A\bar{v}}}\right] \approx C(x,t)\frac{\gamma \alpha k \Gamma}{\rho_s} \quad (54)$$

This is valid if the exponential term is small. The growth rate will then depend on the Γ which implies a growth rate proportional to r. The second scenario will indeed give a significantly less growth rate than the first extreme. As the pore/wormhole grows, Γ and A increases, and α decreases. Since A increases with r^2 and Γ with r, the exponent becomes smaller with increasing wormhole radius. The decrease of α further enhances the decrease of the growth. We therefore expect a change from the first to the second scenario. In conclusion, at some point, the growth rate will go from being proportional to r^2 to r, reducing the growth rate significantly. The part of the wormhole that has not reached this point will continue with the higher growth allowing it to catch up in size. However, as we also see from our experimental results, a uniform radius will not be reached.

6.5 Absorption analysis

6.5.1 Correlating absorption to relevant parameter.

Another way of approaching and analyzing the results and core sample is to make use of the principle behind CT-scanning. X-ray absorption is element specific (heavier elements absorb more than lighter elements) and depends on the density of the particular element. Air shows weak X-ray absorption and rock grains exhibit high absorption. The generated images use grey scale to show different absorption amplitudes. Black areas imply air and hence represent the pore space.

ImageJ [31] is a photo-editing program, which has the feature of measuring the mean grey value in a specified area of the picture. This value, of course, depends on the contrast and brightness settings of the pictures. However, by keeping these settings constant for all images and look at the differences between pre and post scans, makes this method a quantitative tool. To avoid edge effects a small fraction around the whole sample is left out of the specified measuring area. The measured values and the calculated differences can be found in the appendix.

Each scan represents a position along the axial length of the core. Having 74 images implies a distance between images of 1.03 mm along the axis of the sample. In Figure 27, the absorption difference between pre and post CO_2 exposure is plotted as a function of distance along the sample axis. The difference illustrates the change in porosity as a function of distance from the inlet.

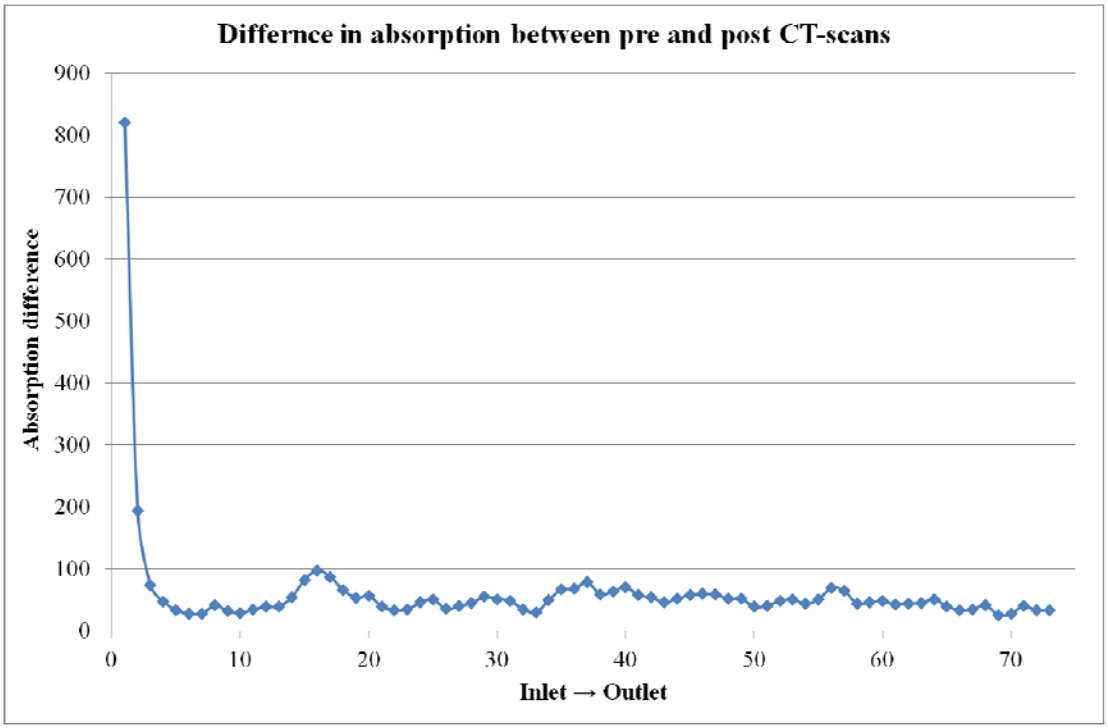

Figure 27: Difference in absorption between pre and post scans with respect of distance along the core.

A high absorption difference indicates an increase of porosity due to calcite dissolution. The change is quite significant at the inlet and a few mm into the sample, while the remaining part of the sample shows a small and nearly constant difference, mainly caused by the wormhole.

What we now want to do is to correlate the absorption to the grain volume of the sample. First, we define:

- 0 absorption implies pore space.
- a_0 and is φ_0 the average absorption value and porosity prior to CO_2 flooding which is related by $a_0 \propto (1- \varphi_0)$.
- a_1 and is φ_1 the absorption and porosity after CO_2 flooding which is related by $a_1 \propto (1- \varphi_1)$.

We then have:

$$a_0 - a_1 \propto [(1 - \varphi_0) - (1 - \varphi_1)] \tag{55}$$

$$\Delta a = a_0 - a_1 \propto [\varphi_1 - \varphi_0] = \Delta\varphi \tag{56}$$

Further on, we normalize the absorption difference by:

$$\frac{\Delta a}{a_0} = \frac{a_0 - a_1}{a_0} = \frac{\varphi_1 - \varphi_0}{1 - \varphi_0} \tag{57}$$

yielding:

$$\Delta\varphi = (\varphi_1 - \varphi_0) = (1 - \varphi_0)\frac{\Delta a}{a_0} \tag{58}$$

The change in mass can then be found by:

$$\Delta m = \rho_{grain} \int (\varphi_1 - \varphi_0) \mathrm{dV} = \rho_{grain} \int (1 - \varphi_0) \frac{\Delta \mathrm{a}}{\mathrm{a}_0} \mathrm{dV} \quad (59)$$

Table 9 contains the calculated change in porosity, grain volume and total mass, together with the corresponding experimental results.

Table 9: Change in grain volume and porosity calculated from the absorption-grain volume correlation and the experimental result.

Parameter	Calculation	Experimental	Deviation
$\Delta\phi$	0.025	0.024	3.6%
ΔV_g	2.12 ml	2.07 ml	3.6%
Δm	5.7 g	5.55 g	3.6%

A deviation of 3.6% between the changes estimated based on the absorption approach and the experimental data is considered acceptable. The present results demonstrate that porosity and mass changes can reasonably well be calculated from CT images taken before and after CO_2 exposure. There is some uncertainty in the density used for converting grain volume into mass because of the density being an average value. However, the resulting error is relatively small.

6.5.2 Exponential fitting

Another way of attempting to describe the dissolution pattern in the core sample is to apply the 1-dimensional reactive flow equation presented in Chapter 2 (Eq. (14)) and try to fit the experimental data in Figure 27. We will not be able to describe the nearly constant offset of the mass change along the sample axis as a result of wormhole formation since 1-dimension, macroscopic, reactive flow model is not able to describe wormholing. However, we want to see if the strong (exponential) decay after a few mm behind the inlet can be interpreted as compact dissolution, which would be described by the 1-dimensional model, or if it reflects the presence of several wormholes that merge into a single wormhole.

Consider the system having a stationary solution $\frac{\partial C}{\partial t} = 0$, and initially being completely saturated with buffered brine. $C(x, t = 0) = C_{eq}$. The boundary condition would be C(x=0, t) = 0. Here, C denotes in this case the calcium concentration in the brine. The injection of fresh brine at the inlet will then result in a concentration gradient similar to the dissolution trend in Figure 27. Two possible extreme cases exist, the first one being completely advection controlled, and the second assuming negligible injection velocity (completely axial diffusion dominance). From literature, we know that convection predominance yields wormholing, while diffusion predominance yields compact dissolution.

If we assume D=0 (first extreme case), a stationary solution ($\frac{\partial C}{\partial t} = 0$) has to fulfill the following equation:

$$0 = -\phi v \frac{\partial C}{\partial x} + Ak\left(1 - \frac{C}{C_{eq}}\right) \quad (60)$$

This type of differential equation is known to have a general solution of:

$$C = C_{eq}[1 - e^{-\alpha x}] \Rightarrow \frac{\partial C}{\partial x} = \alpha C_{eq} e^{-\alpha x} = \alpha(C_{eq} - C) \quad (61)$$

By substituting and rearranging we obtain:

$$k = \frac{\emptyset v C_{eq}}{A} \alpha \quad (62)$$

where v is the Darcy velocity, $\emptyset$ the porosity, C_{eq} the concentration limit, A the surface area of the grain per unit of bulk volume, k the reaction coefficient and α the exponential shape factor. The latter factor is obtained from exponential fitting to the exponential data, Figure 27. As discussed before, the experimental data (change in X-ray absorption) is a measure for the amount of dissolved calcite as a function of distance from the inlet, which, within our model, is proportional to $(1-C/C_{eq})$. I.e. no dissolution if the brine is buffered ($C=C_{eq}$) and maximum dissolution for a non-buffered solution (C=0).

The same approach can be made for the second extreme, v ≈ 0. In this case we end up with:

$$k = \frac{\emptyset D C_{eq}}{A} \alpha^2 \quad (63)$$

A simple Mathematica script, which can be found in the appendix, has been applied for the estimation of α. For both cases we obtain α ≈1.5 mm^{-1}. C_{eq} was set to the average measured Ca^{2+} concentration C_{eq} = 0.031 mol/l (see Chapter 4), v was set to the flow rate used for most of the experiment, v=0.06 ml/min (flow rate #1 in Table 3), D was earlier calculated to D= 3~2 x10^{-9} m^2/s, and porosity and A were measured (φ=0.15, A= 20.42 m^2/cm^3, see Table 2). For both advection and diffusion dominant transport we get k ≈10^{-14} $mol/cm^2/s$. However, as mentioned earlier, the k value for this reaction is expected to be in the range of ~10^{-8} $mol/cm^2/s$. The k value obtained from the fit is considered non-realistic. Therefore, we conclude that the 1-dimensional macroscopic reactive-flow model is not applicable in the present case and that wormholing is the dominating dissolution regime throughout the sample. According to Daccord [15], wormhole growth is impossible to model with a macroscopic model. A microscopic scale must be applied instead, taking the radial diffusion, within each pore, into account. Schechter and Gidley [7] applied a microscopic model (see Chapter 3) and successfully described the wormhole evolution.

6.5.3 Estimating wormhole dimensions

A rough estimate of the wormhole volume can be made based on the X-ray absorption difference data. By assuming that calcite dissolution after about 3 mm, when only a single wormhole prevails, only occur in a wormhole, the difference in absorption for the rest of the sample can be used to estimate the wormhole volume. The assumption is quite weak, and will be a major source of error. The calculated wormhole volume based on this approach is V_{WH} = 1.5 ml which is most likely an over-estimate since dissolution will also occur elsewhere, not only in the wormhole.

ImageJ [31] also features the ability of measuring the area of an arbitrary selection. This can be applied for different estimations regarding the wormhole size. Hence, another approach for the volume estimate is to measure the cross section area in different images with a certain interval between each image. Each measurement

then represents the average cross section at a given position along the sample axis. By assuming a tortuosity factor of 1.2 and integrate the cross-section area along the sample axis, a volume of $V_{WH} = 1.0$ ml is obtained. This is a reasonable result, and as expected it is smaller than the estimate from the average X-ray absorption difference. Increased accuracy could be achieved by higher resolution CT scanning (μCT).

As stated earlier, the wormhole cross section at the outlet is a reasonable representation of the terminal cross section size. Thus, by measuring the cross section area at the outlet we obtain $A_{WH,outlet} = 4.5$ mm^2 giving a terminal radius of $r_{terminal} \approx 1.2$ mm. Note that the uncertainty in this estimate is quite significant, but it gives an idea of the dimensions one can expect the wormhole to have.

7 Conclusion and recommendations

In this work, we have analyzed and interpreted the results of that was carried out with the intention of investigating the reactive transport of CO_2-saturated brine in a carbonate rock. Based on the analysis of the experiment, model calculation performed in this study and a review of previous work, we are able to draw a number of conclusions:

- Flooding a calcite-containing core sample with CO_2 saturated brine results in dissolution of calcite. In most experiments, the dissolution pattern and dominant regime will be of the wormhole-type. To achieve uniform dissolution requires a more advanced experimental procedure, which will be addressed in a following-up project.
- A terminal size is reached for the wormhole with the result of the transition from reaction-controlled to a transport-controlled system. A transport controlled regime implies a rather not completely buffered effluent which is indicated by a drop in the Ca^{2+} concentration.
- The experimentally determined solubility of calcite in CO_2-saturated brine at elevated temperature and pressure turned out to be higher by a factor of 2 than model calculations. For a more accurate estimate of the calcite solubility, we need to have a better understanding of the activity coefficients, the temperature and pressure dependence of the dissociation constants of the involved reactions and the impact of impurities.
- Mass and volume can be obtained from CT-scans taken before and after CO_2 exposure of the sample. X-ray absorption differences yield a reasonable approximation of the amount of dissolved material. A rough estimate of wormhole dimensions can be obtained as well, though the accuracy is limited by the resolution of the CT scanner.
- It was shown that dissolution in carbonate rock cannot be described by a 1D reactive flow model. A microscopic approach is required where also the radial diffusion within each pore is considered.

In future studies, more detailed and advanced measurements should be done. More frequent effluent analysis, continuous CT-scanning to monitor the evolution of the dissolution pattern and a more consistent flow rate should be applied. In a follow-up study, an experiment with the aim of achieving uniform dissolution by the use of retarded acid will be conducted. This will enable the investigation of the uniform dissolution regime, which is relevant for a CO_2 storage situation further away from the injection wells.

Acknowledgments

The author would like to thank Andreas Bauer at the Shell Research Center in Rijswijk and Rune Holt at NTNU & Sintef for supervising me through this project. Further on, great appreciation is also directed to the Shell researchers Suzanne Hangx and Arjan van der Linden for guidance and inputs as well as providing the necessary data and information from the experimental work.
The images made by the researcher Fons Marcelis, who is also the core shed supervisor, at the Shell Research Center in Rijswijk are appreciated.
The author would also like to thank everyone else that has contributed in the present study.

References

[1] Steven S. Zumdahl (2009): “Chemical Principles”. Brooks/Cole

[2] Frederick A. Bettelheim,William H. Brown, Mary K. Campbell, Shawn O. Farrell (2003): “Introduction to General, Organic and Biochemistry”. Brooks/Cole.

[3] C. I. Steefel and K. Maher, “Reviews in mineralogy & geochemistry, volume 70, thermodynamics and kinetics of water-rock interaction,” Mineralogical Society of America & Geochemical Society, (2009).

[4] Pokrovsky, O. S., S. V. Golubev, J. Schott, and A. Castillo (2009a) Calcite, dolomite and magnesite dissolution kinetics in aqueous solutions at acid to circumneutral pH, 25 to 150°C and. Special Issue on CO2 geological sequestration (eds., P. Bénézeth, B. Ménez and C. Noiriel): Chemical Geology, 265, p.20-32.

[5] Pokrovsky, O. S., S. V. Golubev, and G. Jordan, (2009b) Effect of organic and inorganic ligands on calcite and magnesite dissolution rates at 60°C and 30 atm pCO2: Special Issue on CO2 geological sequestration (eds., P. Bénézeth, B. Ménez and C. Noiriel) Chemical Geology, 265, p. 33-43.

[6] Pokrovsky, O. S., S. V. Golubev, and J. Schott (2005) Dissolution kinetics of calcite, dolomite and magnesite at 25°C and 0 to 50 atm pCO2. Chemical Geology, 217, p. 239-255.

[7] Schechter, R. S. and Gidley, J. L.: “The change in pore size distribution from surface reaction in porous media”, A.I.Ch.E. J. (1969), vol. 15, p. 339-350.

[8] L. Niel Plummer and Eurybiades Busenberg: “The solubilities of calcite, aragonite and vaterite in CO_2H_2O solutions between 0 and 90 ^{0}C, and an evaluation of the aqueous model for the system $CaCO_3$-CO_2-H_2O”. U.S. Geological Survey, Mail Stop 432, Reston, Va. 22092

[9] T. Xu, E. Sonnenthal, N. Spycher, and K. Pruess: “Toughreact – a simulation program for non-isothermal multiphase reactive geochemical transport in variably saturated geologic media: Applications to geothermal injectivity and co2 geological sequestration.” Computers & Geosciences, (2006), vol. 32, 145.

[10] Wiebe, R. and V.L. Gaddy: “The solubility in water of carbon dioxide at 50, 75 and 100°C, at pressures to 700 atmospheres”. Journal of the American Chemical Society (1939), vol. 61, p. 315-318.

[11] Duan, Z. and R. Sun: “An improved model calculating CO_2 solubility in pure water and aqueous NaCl solutions from 273 to 533 K and from 0 to 2000 bar.” Chemical Geology (2003), 193, p. 257-271.

[12] Christman, P.G. and Edgar, T.F.: “Distributed pore-size model for sulfation of limestone”, AIChE Journal (May 1983), vol. 29, n°3, p. 388-395.

[13] Hendrickson, A. R., R. B. Rosene, and D. R. Wieland, paper presented at the American Chemical Society meeting, Cleveland (April, 1960).

[14] Rowan, G., J. Inst. Petrol. (1959), vol. 45, 431.

[15] Daccord, G., Lenormand, R. and Lietard, O.: “Chemical dissolution of a porous medium by a reactive fluid – I: Model for the wormholing phenomenon”, Chem. Eng. Sci. (1993), vol. 48, n°1, p. 169-178.

[16] Daccord, G., Touboul, E., Lenormand, R.: “Carbonate acidizing: toward a quantitative model of the wormholing phenomenon”, SPE Production Engineering (February 1989), p. 63-68.

[17] Levich V.G (1962): “Physicochemical Hydrodynamics”, Englewood Cliffs: Prentice Hall Inc., NJ 55, 70.
[18] Daccord, G.: "Chemical Dissolution of a Porous Medium by a Reactive Fluid," Phys. Rev. Lett. (1987), vol. 58, 479-82.
[19] Ball, R.C.: "DLA in the Real World," On Growth and Form, H.E. Stanley and N. Ostrowsky (eds.), Martinus Nijhoff, Dordrecht (1986), p. 74-75.
[20] P. Egermann, S. Bekri and O. Vizika: “An Integrated Approach to assess the petrophysical properties of rocks altered by rock/fluid interactions (CO_2 injection)”, Institut Français du Pétrole (IFP) (1995).
[21] Grigg, R.B. and Svec, R.K.: “Co-injeted CO2-brine interactions with Indiana Limestone”, paper SCA 2003-19 presented at the Society of Core Analysts Symposium, September 21-24 2003, Pau, France.
[22] Svec, R.K. and Grigg, R.B.: “Physical effects of WAG fluids on carbonate core plugs”, paper SPE 71496 presented at the Annual Technical Conference and Exhibition, 30 September- 3 October 2001, New Orleans, LA.
[23] Mathis, R.L., Sears, S.O.: “Effect of CO2 flooding on dolomite reservoir rock, Denver Unit, Wasson (San Andres) field, TX”, paper SPE 13132 presented at the Annual Technical Conference and Exhibition, September 16-19 1984, Houston, TX.
[24] Kane, A.V.: “Performance review of a large-scale CO2-WAG enhanced recovery project, SACROC Unit – Kelly-Snyder field”, JPT (February 1979), p. 217-231.
[25] Kamath, J ., Nakagawa, F.M., Boyer, R.E. and Edwards, K.A..: “Laboratory Investigation of Injectivity Losses during WAG in West Texas Dolomites”, paper SPE 39791 presented at the Permian Basin Oil and Gas Conference, 23 - 26 March 1998, Midland, TX.
[26] Christman, P.G. , Gorell, S.B.: “Comparison of laboratory and field observed CO2 tertiary injectivity”, JPT (February 1990), p. 226-233.
[27] Prieditis, J., Wolle, C.R., and Notz, P.K.: “A laboratory and field injectivity study: CO2 WAG in the Saan Andres formation of Wast Texas”, paper SPE 22653 presented at the Annual Technical Conference and Exhibition, 6-9 October 1991, Dallas, TX.
[28] Békri, S., Thovert, J.-F., Adler, P.M.: “Dissolution of porous media”, Chem. Eng. Sci.,(1995) 50, 17, p. 2765-2791.
[29] Békri, S., Thovert, J.-F., Adler, P.M.: “Dissolution and deposition in fractures”, Eng. Geol., (1997) 48, p. 283-308.
[30] Laroche, C., and Vizika, O.: “Two-Phase flow properties prediction from small-scale data using pore-network modeling”, Transport in Porous Media (October 2005), vol. 61, n°1, p. 77-91.
[31] ImageJ is a freeware developed at the National Institutes of Health by an employee of the Federal Government. The software is not subject to copyright protection.

The solubility of Calcium Carbonat ($CaCO_3$)

This program consists of two parts, both aiming for the calculation of the solubility of calcium carbonate in the presens of carbon dioxid. The first part involves a open system, involving that the solution always is in contact and CO_2 equilibrium with the air. This allows more CO_2 to dissolve into the solution. The second part involvs a closed system, meaning no contact with air. This removes all external sources of CO_2.

The two parts differs both in the base equations and the initialization. The first part is as mentioned an open system always in contact with air, thus equilibrium between air and solution is always fulfilled. The second part is a closed system, having a fixed initial consentration of CO_2. The first part therefore bases it's calculation on a defined partial pressure for each particular run, whereas the second part base the calcualtions on the defined initial consentration of CO_2. Both part are design to run a certain number of calcualtions with increasing partial pressure or initial consentration from calculation to calculation.
The result from the first part is written to a .xls file named solubility1.xls, while the second part is written to solubility2.xls.

*NOTE: The partial pressure cannot be set to zero in the first part. This condition correspond to a closed system with no initial consentration of CO_2 in the solution.

PART 1 - OPEN SYSTEM

The system is based on the following reactions and balances:

- Carbonic Acid : $H_2O + CO_2 \Rightarrow H^+ + HCO_3^-$, Ka1
- Dissolution of Calcium Carbonate: $H^+ + Ca_2CO_3 \Rightarrow Ca^{2+} + CO_3^{2-}$, K
- Water dissociation: $H_2O \Rightarrow H^+ + OH^-$, Kw
- Electricity Balance: $2Ca^{2+} + H^+ = HCO_3^- + OH^-$
- Henry's law: $\frac{P_{CO_2}}{[CO_2]} = K_H$

```
Clear["Global`*"]

Ka1 = 5.13 * 10^-7 ;
Kw = 1.0 * 10^-14 ;
KH = 60.88;
K = 24.27 ;
Pco2 = 70;
ɣ = 1.0;
runs = 4;

Off[Solve::ratnz]

results = Array[0 &, {runs + 2, 8}];
results[[1, 1]] = "Run";
```

```
results[[2, 1]] = " ";
For[i = 2, i < 9, i++,

  results[[2, i]] = "[mol/l]"];

results[[1, 2]] = "PCO2";
results[[1, 3]] = "Calcium";
results[[1, 4]] = "Hydrogen";
results[[1, 5]] = "Bicarbonate";
results[[1, 6]] = "CO2";
results[[1, 7]] = "OH";
results[[1, 8]] = "pH";

For[j = 3, j < runs + 3, j++,

  Clear[hydro, calcium, oh, hco3, co2];

  solution = Solve[(calcium * ɣ) * (hco3 * ɣ) / (hydro * ɣ) / K == 1 &&
     (hydro * ɣ) * (hco3 * ɣ) / (co2 * ɣ) / Ka1 == 1 &&
     ((hydro * ɣ) * (oh * ɣ)) / Kw == 1 && 2 * calcium + hydro - hco3 - oh == 0 &&
     Pco2 / (co2 * ɣ) / KH == 1, {calcium, hydro, hco3, co2, oh}];

  calcium = calcium /. solution;
  hydro = hydro /. solution;
  hco3 = hco3 /. solution;
  co2 = co2 /. solution;
  oh = oh /. solution;

  n = Length[solution];
  solutionexist = False;

  For[i = 1, i < n , i++, test1 = Positive[hydro[[i]]]; test2 = Positive[calcium[[i]]];
   test3 = Positive[hco3[[i]]]; test4 = Positive[co2[[i]]]; test5 = Positive[oh[[i]]];
   If[test1 == True && test2 == True && test3 == True && test4 == True && test5 == True,
    solutionexist = True ; Break[]]];

  If[solutionexist == False && i < 1, Print["No solution"]];

  calcium = calcium[[i]];
  hydro = hydro[[i]];
  hco3 = hco3[[i]];
  co2 = co2[[i]];
  oh = oh[[i]];

  results[[j, 1]] = j - 2;
  results[[j, 2]] = Pco2;
  results[[j, 3]] = calcium;
  results[[j, 4]] = hydro;
  results[[j, 5]] = hco3;
  results[[j, 6]] = co2;
  results[[j, 7]] = oh;
  results[[j, 8]] = -Log10[hydro];

  ɣ = ɣ - 0.1;
 ];
Export["solubility_open.xls", results];
```

PART 2 - CLOSED SYSTEM

Theory behind the solution

The system is based on the following reactions and balances:

- Carbonic Acid : $H_2O + CO_2 \Rightarrow H^+ + HCO_3^-$, Ka1
- Dissolution of Calcium Carbonate: $H^+ + Ca_2CO_3 \Rightarrow Ca^{2+} + CO_3^{2-}$, K
- Water dissociation: $H_2O \Rightarrow H^+ + OH^-$, Kw
- Electricity Balance: $2Ca^{2+} + H^+ = HCO_3^- + OH^-$
- Carbon Stoichiometry Balance: $Ca^{2+} + CO_{2,i} = CO_{2,eq} + HCO_3^-$

```
Clear["Global`*"]

Ka1 = 5.13 * 10^-7 ;
Kw = 1.0 * 10^-14 ;
K = 24.27 ;
co2i = 1.22;
ɣ = 1.0;
runs = 4;

Off[Solve::ratnz]

results = Array[0 &, {runs + 2, 8}];
results[[1, 1]] = "Run";
results[[2, 1]] = " ";
For[i = 2, i < 9, i++,

  results[[2, i]] = "[mol/l]"];

results[[1, 2]] = "CO2_i";
results[[1, 3]] = "Calcium";
results[[1, 4]] = "Hydrogen";
results[[1, 5]] = "Bicarbonate";
results[[1, 6]] = "CO2";
results[[1, 7]] = "OH";
results[[1, 8]] = "pH";

For[j = 3, j < runs + 3, j++,

  Clear[hydro, calcium, oh, hco3, co2];

  solution = Solve[(calcium * ɣ) * (hco3 * ɣ) / (hydro * ɣ) / K == 1 &&
     (hydro * ɣ) * (hco3 * ɣ) / (co2 * ɣ) / Ka1 == 1 &&
     ((hydro * ɣ) * (oh * ɣ)) / Kw == 1 &&  2 * calcium + hydro - hco3 - oh == 0 &&
     calcium + co2i - co2 - hco3 == 0, {calcium, hydro, hco3, co2, oh}];

  calcium = calcium /. solution;
  hydro = hydro /. solution;
  hco3 = hco3 /. solution;
  co2 = co2 /. solution;
  oh = oh /. solution;

  n = Length[solution];
  solutionexist = False;

  For[i = 1, i < n , i++, test1 = Positive[hydro[[i]]]; test2 = Positive[calcium[[i]]];
```

```
    test3 = Positive[hco3[[i]]]; test4 = Positive[co2[[i]]]; test5 = Positive[oh[[i]]];
    If[test1 == True && test2 == True && test3 == True && test4 == True && test5 == True,
     solutionexist = True ; Break[]]];

  If[solutionexist == False && i < 1, Print["No solution"]];

  calcium = calcium[[i]];
  hydro = hydro[[i]];
  hco3 = hco3[[i]];
  co2 = co2[[i]];
  oh = oh[[i]];

  results[[j, 1]] = j - 2;
  results[[j, 2]] = co2i;
  results[[j, 3]] = calcium;
  results[[j, 4]] = hydro;
  results[[j, 5]] = hco3;
  results[[j, 6]] = co2;
  results[[j, 7]] = oh;
  results[[j, 8]] = -Log10[hydro];

  𝔵 = 𝔵 - 0.1;
 ];
Export["solubility_colsed.xls", results];
```

EXPONENTIAL FIT

The scripts performs a expontial fitting to the values assigned to the variable "data".

```
Clear["Global`*"];

(*The data variable needs to be defined. The
  content should be the image number as x-values
  and the corresponding difference as y-value*)
data = (*Must be specified*)

  model = h + b * Exp[-a * x];

fit = NonlinearModelFit[data, model, {h, b, {a, .01}}, x];
bestfit = fit["BestFitParameters"];

h = h /. bestfit[[1]];
b = b /. bestfit[[2]];
a = a /. bestfit[[3]];

ListLinePlot[data, AxesOrigin → {0, 0},
  PlotRange -> {0, 1000}, PlotStyle → {Thick}, ImageSize → 500,
  PlotLabel → Style["Line plot of data", 16], LabelStyle → Directive[12, Bold]]

modelf = Function[{x}, Evaluate[model /. bestfit]];

result = Array[0 &, {5, 2}];
result[[1, 1]] = "Parameter";
result[[1, 2]] = "Value";
result[[2, 1]] = "a";
result[[2, 2]] = a;
result[[3, 1]] = "b";
result[[3, 2]] = b;
result[[4, 1]] = "h";
result[[4, 2]] = h;
result[[5, 1]] = "Equation";
result[[5, 2]] = "h+b*e^-ax";

Plot[modelf[x], {x, 1, 74}, AxesOrigin → {0, 0}, PlotRange → All,
 Epilog → Map[Point, data], PlotStyle → {Thick}, ImageSize → 500,
 PlotLabel → Style["Plot of fitted function and data points", 16],
 LabelStyle → Directive[12, Bold]]

Export["Exponential_fit.txt", result, "Table"];
```

	Measured Data			
Injection Point	Pre	Post	Difference	Upscale
1	2295.675	1475.745	819.93	903.51
2	2368.913	2175.714	193.199	212.89
3	2376.429	2302.835	73.594	81.10
4	2383.413	2336.375	47.038	51.83
5	2391.418	2358.52	32.898	36.25
6	2386.062	2358.586	27.476	30.28
7	2382.501	2355.503	26.998	29.75
8	2371.255	2330.575	40.68	44.83
9	2343.09	2311.145	31.945	35.20
10	2345.985	2318.054	27.931	30.78
11	2359.206	2325.117	34.089	37.56
12	2358.655	2320.26	38.395	42.31
13	2365.422	2326.327	39.095	43.08
14	2351.339	2297.8	53.539	59.00
15	2337.97	2255.821	82.149	90.52
16	2322.985	2225.831	97.154	107.06
17	2314.955	2228.375	86.58	95.41
18	2317	2251.305	65.695	72.39
19	2353.082	2300.028	53.054	58.46
20	2358.521	2302.724	55.797	61.48
21	2348.825	2309.896	38.929	42.90
22	2348.222	2315.845	32.377	35.68
23	2356.665	2322.508	34.157	37.64
24	2350.84	2305.767	45.073	49.67
25	2320.957	2270.864	50.093	55.20
26	2306.817	2272.236	34.581	38.11
27	2329.021	2289.763	39.258	43.26
28	2344.998	2300.892	44.106	48.60
29	2349.778	2295.253	54.525	60.08
30	2332.963	2282.388	50.575	55.73
31	2326.875	2278.923	47.952	52.84
32	2332.757	2298.312	34.445	37.96
33	2349.474	2320.138	29.336	32.33
34	2368.208	2319.594	48.614	53.57
35	2379.657	2313.177	66.48	73.26
36	2378.696	2311.524	67.172	74.02
37	2362.612	2284.551	78.061	86.02
38	2347.062	2288.494	58.568	64.54
39	2350.194	2287.497	62.697	69.09
40	2342.192	2271.87	70.322	77.49
41	2335.829	2279.17	56.659	62.43
42	2349.56	2296.121	53.439	58.89
43	2360.247	2315.289	44.958	49.54
44	2363.835	2312.045	51.79	57.07
45	2355.176	2298.466	56.71	62.49
46	2352.727	2293.586	59.141	65.17
47	2344.709	2286.564	58.145	64.07
48	2341.185	2289.801	51.384	56.62
49	2333.935	2282.536	51.399	56.64
50	2329.3	2291.142	38.158	42.05
51	2341.466	2301.297	40.169	44.26
52	2344.18	2296.417	47.763	52.63
53	2339.545	2289.72	49.825	54.90
54	2345.714	2302.883	42.831	47.20
55	2359.633	2309.722	49.911	55.00
56	2355.211	2286.711	68.5	75.48
57	2334.072	2269.528	64.544	71.12
58	2334.693	2291.16	43.533	47.97
59	2346.129	2300.289	45.84	50.51
60	2366.716	2319.356	47.36	52.19
61	2362.465	2320.678	41.787	46.05
62	2363.406	2319.666	43.74	48.20
63	2361.792	2317.417	44.375	48.90
64	2358.885	2308.665	50.22	55.34
65	2360.231	2321.319	38.912	42.88
66	2363.045	2329.788	33.257	36.65
67	2372.862	2339.208	33.654	37.08
68	2369.929	2328.662	41.267	45.47
69	2362.3	2337.683	24.617	27.13
70	2379.495	2352.215	27.28	30.06
71	2373.743	2333.92	39.823	43.88
72	2358.579	2326.405	32.174	35.45
73	2364.128	2330.965	33.163	36.54
74	2312.709	2117.649	195.06	214.94

DIFFUSION MODEL

$$\varphi \frac{\partial C}{\partial t} = -\varphi v \frac{\partial C}{\partial x} + \varphi D \frac{\partial^2 C}{\partial x^2} + Ak(1 - \frac{C}{C_{eq}})$$

Assuming stationary solution and negligible convection →

$$0 = \varphi D \frac{\partial^2 C}{\partial x^2} + Ak(1 - \frac{C}{C_{eq}})$$

$$\varphi D \frac{\partial^2 C}{\partial x^2} = -Ak(1 - \frac{C}{C_{eq}})$$

$$C = C_{eq}[1 - e^{-\alpha x}] \Rightarrow C'' = -\alpha^2 C_{eq} e^{-\alpha x}$$

$$C_{eq} = C + C_{eq} e^{-\alpha x} \Rightarrow C'' = \alpha^2 \left(C - C_{eq}\right) = \frac{B}{C_{eq}} C - B$$

$$B = \alpha^2 C_{eq} \Rightarrow \alpha = \sqrt{\frac{B}{C_{eq}}} = \sqrt{\frac{Ak}{\varphi D C_{eq}}} \Rightarrow k = \frac{\varphi D C_{eq}}{A} \alpha^2$$

CONVECTION MODEL

$$\varphi \frac{\partial C}{\partial t} = -\varphi v \frac{\partial C}{\partial x} + \varphi D \frac{\partial^2 C}{\partial x^2} + Ak(1 - \frac{C}{C_{eq}})$$

Assuming stationary solution and negligible diffusion →

$$0 = -\varphi v \frac{\partial C}{\partial x} + Ak(1 - \frac{C}{C_{eq}})$$

$$\varphi v \frac{\partial C}{\partial x} = Ak(1 - \frac{C}{C_{eq}})$$

$$C = C_{eq}[1 - e^{-\alpha x}] \Rightarrow C' = \alpha C_{eq} e^{-\alpha x}$$

$$C_{eq} = C + C_{eq} e^{-\alpha x} \Rightarrow C' = \alpha \left(C - C_{eq}\right) = B - \frac{B}{C_{eq}} C$$

$$B = \alpha C_{eq} \Rightarrow \alpha = \frac{B}{C_{eq}} = \frac{Ak}{\varphi v C_{eq}} \Rightarrow k = \frac{\varphi v C_{eq}}{A} \alpha$$

D= Diffusion Coefficient *[m^2/s]*
v= Darcy velocity *[m/s]*
φ= Porosity
A= Grain area per pore volume unit *[m^3/m^2]*
C= Concentration
α= Exponential shape factor *[m^{-1}]*